

# The cell-type specific connectivity of the local cortical network explains prominent features of neuronal activity

Tobias C. Potjans<sup>1,2,3</sup>, Markus Diesmann<sup>1,2,4</sup>

<sup>1</sup>Institute of Neuroscience and Medicine (INM-6)  
Computational and Systems Neuroscience  
Research Center Juelich, 52425 Juelich, Germany

<sup>2</sup>Brain and Neural Systems Team  
RIKEN Computational Science Research Program  
Wako-shi, Saitama 351-0198, Japan

<sup>3</sup>Faculty of Biology III  
Albert-Ludwigs-University Freiburg  
Schaenzlestrasse 1, 79104 Freiburg, Germany

<sup>4</sup>RIKEN Brain Science Institute  
Wako-shi, Saitama 351-0198, Japan

## Abstract

In the past decade, the cell-type specific connectivity and activity of local cortical networks have been characterized experimentally to some detail. In parallel, modeling has been established as a tool to relate network structure to activity dynamics. While the available connectivity maps have been used in various computational studies, prominent features of the simulated activity such as the spontaneous firing rates do not match the experimental findings. Here, we show that the inconsistency arises from the incompleteness of the connectivity maps. Our comparison of the most comprehensive maps (Thomson et al., 2002; Binzegger et al., 2004) reveals their main discrepancies: the lateral sampling range and the specific selection of target cells. Taking them into account, we compile an integrated connectivity map and analyze the unified map by simulations of a full scale model of the local layered cortical network. The simulated spontaneous activity is asynchronous irregular and the cell-type specific spontaneous firing rates are in agreement with *in vivo* recordings in awake animals, including the low rate of layer 2/3 excitatory cells. Similarly, the activation patterns evoked by transient thalamic inputs reproduce recent *in vivo* measurements. The correspondence of simulation results and experiments rests on the consideration of specific target type selection and thereby on the integration of a large body of the available connectivity data. The cell-type specific hierarchical input structure and the combination of feed-forward and feedback connections reveal how the interplay of excitation and inhibition shapes the spontaneous and evoked activity of the local cortical network.

## Introduction

The local cortical network is considered a building block of brain function and over the last century, the hypothesis that the interactions of neurons within the microcircuit are governed by the cell-type specific connectivity has been refined (see e.g. [Douglas & Martin \(2007a,b\)](#) for reviews). In the last decade, progress in methodology enabled the compilation of comprehensive connectivity maps: [Thomson et al. \(2002\)](#) used electrophysiological recordings to estimate the connection probabilities between various cell types in layers 2/3, 4 and 5 in slices of rat and cat neocortex. Shortly thereafter, [Binzegger et al. \(2004\)](#) applied a modified version of Peters' rule ([Braitenberg & Schüz, 1998](#)) to derive the cell-type specific distribution of synapses from morphological reconstructions of *in vivo* labeled cells from area 17 of the cat. These approaches entail partly contradicting results ([Thomson & Lamy, 2007](#)), but the compatibility of these maps and the influence of the different methodologies have not been quantitatively assessed.

Due to recent advances in *in vivo* electrophysiology and two-photon optical imaging, the structural data can now be contrasted with observations of the dynamics. Characteristic features are the cell-type specific firing rates during ongoing activity in awake animals: low pyramidal neuron firing rates below 1Hz are reported in layer 2/3 (L2/3) and highest rates in L5 (e.g. [Greenberg et al., 2008](#); [de Kock & Sakmann, 2009](#)).

Early network models already incorporate basic anatomy and electrophysiology such as the separation of excitatory and inhibitory cell types and a sparse, seemingly random connectivity ([Amit & Brunel, 1997](#); [van Vreeswijk & Sompolinsky, 1996](#)). The balance of excitation and inhibition explains the asynchronous irregular (AI) spiking activity and the large membrane potential fluctuations observed *in vivo*. Models eventually incorporated multiple cell types to capture layer-specific connections (e.g. [Hill & Tononi, 2005](#); [Traub et al., 2005](#)) and employ data based connectivity maps ([Haeusler & Maass, 2007](#); [Haeusler et al., 2009](#); [Heinze et al., 2007](#); [Izhikevich & Edelman, 2008](#); [Binzegger et al., 2009](#)). However, no study to date reported cell-type specific firing rates consistent with the experimental observations. *A priori* it is unclear whether this is due to a misinterpretation of the raw connectivity data or due to further model assumptions. Since the studies comprise networks based on point-neuron as well as on multi-compartment neuron models, the mismatch in fundamental characteristics like stationary firing rates is unlikely to be caused by a lack in complexity of the network elements but rather by the incompleteness of the connectivity map.

In the present study we quantify the discrepancies between the electrophysiological and anatomical connectivity maps to systematically compile an integrated map. To resolve conflicts, we additionally incorporate insights from photostimulation ([Dantzker & Callaway, 2000](#); [Zarrinpar & Callaway, 2006](#)) and electron microscopy ([McGuire et al., 1984](#)) studies, reporting the specific selection of interneurons by a subset of inter-layer projections. We then check the consistency of structure and activity by means of full scale simulations of the local cortical network.

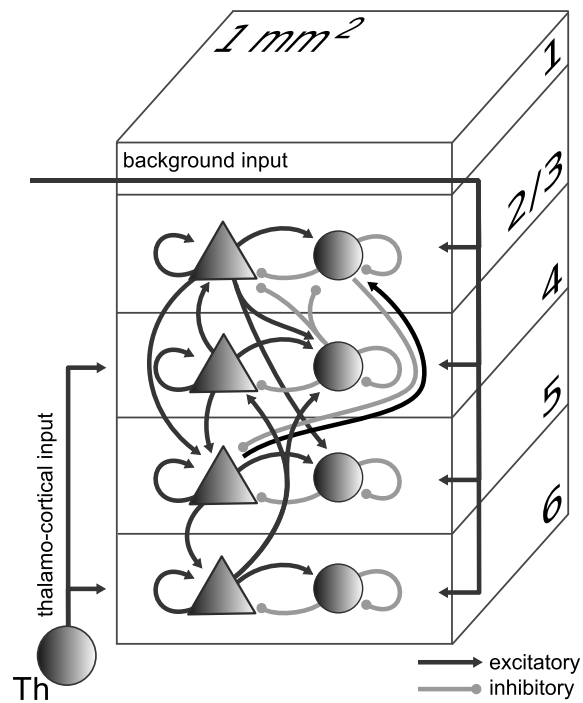


**Figure 1:** Model definition. Layers 2/3, 4, 5 and 6 are each represented by an excitatory (triangles) and an inhibitory (circles) population of model neurons. The number of neurons in a population is chosen according to Binzegger et al. (2004) based on the countings of Beaulieu & Colonnier (1983); Gabbott & Somogyi (1986). Input to the populations is represented by thalamo-cortical input targeting layers 4 and 6 and background input to all populations. Excitatory (black) and inhibitory (gray) connections with connection probabilities  $> 0.04$  are shown. The model size corresponds to the cortical network below  $1 \text{ mm}^2$  surface.

## Materials and Methods

The network model (Fig. 1) represents four layers of cortex, L2/3, L4, L5 and L6, each consisting of two populations of excitatory (e) and inhibitory (i) neurons. Throughout the article, we use the term *connection* with reference to populations, defined by the pre- and postsynaptic layers and neuron types. The term *projection* is used for the two connections of a single presynaptic population to both populations of a target layer. A connectivity map is defined by the sixty-four connection probabilities between the eight considered cell types.

### Connectivity data

For the anatomical map (a), [Binzegger et al. \(2004\)](#) provide the relative number of synapses participating in a connection and the total absolute number of synapses, depending on pre- and postsynaptic type, of area 17 (supplementary Table 6). The product of these measures gives the absolute number of synapses  $K$  for any connection. To calculate the corresponding connection probabilities  $C_a$  we assume that the synapses are randomly distributed allowing multiple contacts between any two neurons. With  $N^{\text{pre(post)}}$  being the number of neurons in the presynaptic (postsynaptic) population:

$$C_a = 1 - \left(1 - \frac{1}{N^{\text{pre}} N^{\text{post}}}\right)^K. \quad (1)$$

The often used expression

$$C_a = K/N^{\text{pre}} N^{\text{post}} \quad (2)$$

is the corresponding first-order Taylor series approximation and valid for small  $K/(N^{\text{pre}} N^{\text{post}})$  (see *Supplemental Material*). The original published data constitute our raw connectivity map ([Binzegger et al. \(2004\)](#), their figure 12). Consistent with other modeling work ([Izhikevich & Edelman, 2008](#)), we construct an improved (“modified”) anatomical map by assigning the unassigned symmetric (inhibitory) synapses, originating from a potential underestimation of interneuronal connectivity, to within-layer projections originating from local interneurons ([Binzegger et al., 2004](#)). The derived connection probabilities are inversely proportional to the considered surface area  $\pi r^2$  (Fig. 2B). This can be easily understood when considering the approximation eq. (2): the numbers of neurons  $N$  and synapses  $K$  increase linear with the surface area and therefore  $C_a \propto \pi r^2 / (\pi r^2)^2 = 1/\pi r^2$ . The product of the connection probability and the surface area is constant for large areas (Fig. 2B). Hence, we use throughout this article the area-corrected connection probability  $\tilde{C}_a = \lim_{r \rightarrow \infty} C_a \pi r^2$  for all numerical values of the anatomical map.

The physiological hit rate estimates ([Thomson et al. \(2002\)](#), their Table 1) provide the physiological map (p). We combine multiple independently measured hit rates for the same connection by a weighted sum

$$C_p = \sum_i R_i Q_i / \sum_j Q_j, \quad (3)$$

where  $R_i$  and  $Q_i$  are the hit rate and the number of tested pairs in the  $i$ th experiment, respectively. In accordance with [Haeusler & Maass \(2007\)](#), we set the probabilities of the L2/3i to L5e and of the L4i to L2/3i connections to 0.2. While

these data constitute the raw map, we incorporate additional hit rate estimates (Table 1) to create an improved (modified) physiological connectivity map. The numerical values of all connectivity maps are listed in supplementary Table 6.

We classify all connections into two main groups: recurrent intra-layer or “within-layer” connections and connections between different layers or “inter-layer” connections.

### Lateral connectivity model

We use a Gaussian model for describing the lateral connection probability profile

$$C(r) = C_0 \exp\left(\frac{-r^2}{2\sigma^2}\right). \quad (4)$$

with  $r$  being the lateral distance and  $C_0$  and  $\sigma$  specifying the peak connection probability (zero lateral distance) and the lateral spread of connections, respectively. Thereby, we assume that the underlying lateral connectivity is the same for both connectivity maps, i.e. that  $C_0$  and  $\sigma$  are universal. Furthermore, we assume that the experimental data correspond to a random sampling of connections within a cylinder of a fixed sampling radius  $r_a > r_p$  and corresponding mean connection probabilities  $C_{a/p} = 1/(\pi r_{a/p}^2) \int_0^{r_{a/p}} \int_0^{2\pi} C(r) r dr d\varphi = 2\pi C_0 \sigma^2 / (\pi r_{a/p}^2) [1 - \exp(-r_{a/p}^2 / 2\sigma^2)]$ . These expressions for the mean connection probabilities of the two connectivity maps allow us to determine the two unknown parameters  $C_0$  and  $\sigma$ . We obtain in closed form (see *Supplemental Material*)

$$\sigma = r_p \left[ -2 \ln \left( 1 - \frac{\pi r_p^2 C_p}{\tilde{C}_a} \right) \right]^{-1/2} \quad (5)$$

and

$$C_0 = \frac{\tilde{C}_a}{2\pi\sigma^2}. \quad (6)$$

In principle, this approach may be applied to an individual connection. However, the sampling radius is the same for all connections of a map. Therefore we determine  $\sigma$  and  $C_0$  only for the global mean connection probabilities of the two maps which provides robustness against uncertainties in the probability estimate of a particular connection.

The simulations use a laterally uniform connectivity profile, i.e. the connectivity between two neurons is exclusively determined by the cell-types and not their location in space. The mean connection probability of the model  $C_m$  depends on the size of the network (e.g. the surface area  $\pi r_m^2$ ) and the parameters of the lateral model, but by applying eqs. (5) and (6) it can also be expressed in terms of the experimentally accessible parameters  $C_p$ ,  $r_p$  and  $\tilde{C}_a$

$$\begin{aligned} C_m &= \frac{1}{\pi r_m^2} \int_0^{r_m} \int_0^{2\pi} C(r) r dr d\varphi \\ &= \frac{2}{r_m^2} C_0 \sigma^2 [1 - \exp(-r_m^2 / (2\sigma^2))] \\ &= \frac{\tilde{C}_a}{\pi r_m^2} \left[ 1 - (1 - \pi r_p^2 \tilde{C}_p / \tilde{C}_a)^{r_m^2 / r_p^2} \right]. \end{aligned} \quad (7)$$

where  $\bar{C}_p$ , and  $\bar{C}_a$  specify the global means. To arrive at the individual connection probabilities at a given model size it is sufficient to multiply a connectivity map by the ratio of  $C_m$  and the global mean of the map  $\bar{C}_{a/p}$ .

Table 1: Modified physiological connectivity map. The map incorporates hit rate estimates of several studies. The selection of studies is based on the comprehensive review by [Thomson & Lamy \(2007\)](#) including all data where hit rate and the number of tested pairs can be extracted such that [eq. \(3\)](#) is applicable. The table lists, from left to right, connection specifier, number of existing connections (product of hit rate and number of tested pairs), number of tested pairs and the publication from which the data are extracted. A star (\*) indicates that the number of tested pairs is not explicitly given, but estimated from the stated accuracy of connection probability. Furthermore, we use the following additional data on within-layer connections that is not reported separately. [Thomson et al. \(1996\)](#); [Thomson & Lamy \(2007\)](#): i to e in L2/3, L4 and L5 21 connected of 93 tested pairs; [Ali et al. \(2007\)](#): i to e in L2/3, L4 and L5 30 connected of 90 tested pairs, e to i in L2/3, L4 and L5 21 connected of 48 tested pairs; i to e in L2/3 and L4 9 connected of 69 tested pairs and e to i in L2/3 and L4 21 connected of 147 tested pairs. The reported numbers of connected and tested pairs are uniformly distributed to the reported layers.

connection	existing	tested	publication
L2/3e→L2/3e	65	247	<a href="#">Thomson et al. (2002)</a> (rat)
	8	81	<a href="#">Thomson et al. (2002)</a> (cat)
	8	32	<a href="#">Bannister &amp; Thomson (2007)</a> (rat)
	3	36	<a href="#">Bannister &amp; Thomson (2007)</a> (cat)
	48	549	<a href="#">Mason et al. (1991)</a>
	32	305	<a href="#">Kapfer et al. (2007)</a>
	22	112	<a href="#">Yoshimura et al. (2005)</a>
	63	760	<a href="#">Holmgren et al. (2003)</a>
	24	110	<a href="#">Ren et al. (2007)</a>
L2/3e→L2/3i	6	25	<a href="#">Thomson et al. (2002)</a> (cat)
	22	107	<a href="#">Thomson et al. (2002)</a> (rat)
	151	243	<a href="#">Holmgren et al. (2003)</a>
	19	40	<a href="#">Kapfer et al. (2007)</a> (FS)
	29	100	<a href="#">Kapfer et al. (2007)</a> (SOM)
L2/3i→L2/3e	7	25	<a href="#">Thomson et al. (2002)</a> (cat)
	17	107	<a href="#">Thomson et al. (2002)</a> (rat)
	136	243	<a href="#">Holmgren et al. (2003)</a>
	26	39	<a href="#">Kapfer et al. (2007)</a> (FS)
	19	39	<a href="#">Kapfer et al. (2007)</a> (SOM)
L2/3i→L2/3i	2	2	<a href="#">Thomson et al. (2002)</a> (cat)
	2	8	<a href="#">Thomson et al. (2002)</a> (rat)
L4e→L4e	10	139	<a href="#">Bannister &amp; Thomson (2007)</a> (cat)
	22	528	<a href="#">Bannister &amp; Thomson (2007)</a> (rat)

connection	existing	tested	publication
L4e → L4i	4	23	Thomson et al. (2002)
	131	655	Feldmeyer et al. (2005)
	11	89	Beierlein et al. (2003)
	25	234	Maffei et al. (2004)
L4i → L4e	8	42	Thomson et al. (2002)
	3	21	Ali et al. (2007) (nonFS)
	11	154	Ali et al. (2007) (FS)
	74	172	Beierlein et al. (2003) (FS)
	36	63	Beierlein et al. (2003) (LTS)
L4i → L4i	10	64	Ali et al. (2007) (nonFS)
	10	40	Ali et al. (2007) (FS)
	83	190	Beierlein et al. (2003) (FS)
	26	74	Beierlein et al. (2003) (LTS)
	4	42	Thomson et al. (2002)
L5e → L5e	3	6	Thomson et al. (2002)
L5e → L5i	15	163	Thomson et al. (2002)
	50	500	Markram et al. (1997)
	218	1655	Le Be & Markram (2006)
	29	206	Le Be & Markram (2006)
	148	1233	Wang et al. (2006)
	26	260	Wang et al. (2006)
	173	1450	Silberberg & Markram (2007)
L5i → L5e	19	190	Thomson (1997); Thomson & Deuchars (1997)*
	6	79	Thomson et al. (1995)
	7	73	Thomson et al. (2002)
L5i → L5i	9	73	Thomson et al. (2002)
L6e → L6e	56	1512	Mercer et al. (2005)
	4	204	Beierlein & Connors (2002)
L6e → L6i	8	38	West et al. (2006) (cat)
	5	21	West et al. (2006) (rat)
L2/3e → L4e	0	25	Thomson et al. (2002) (rat)
	0	70	Thomson et al. (2002) (cat)
L2/3e → L4i	1	12	Thomson et al. (2002) (rat)
	7	37	Thomson et al. (2002) (cat)
L2/3i → L4e	0	29	Thomson et al. (2002) (rat)
	0	10	Thomson et al. (2002) (cat)
L2/3e → L5e	2	2	Thomson et al. (2002) (cat)
	16	29	Thomson et al. (2002) (rat)
	25	259	Thomson & Bannister (1998)
	247	1324	Kampa et al. (2006)
L4e → L2/3e	10	50	Yoshimura et al. (2005)
	7	25	Thomson et al. (2002) (rat)
	7	70	Thomson et al. (2002) (cat)
	64	640	Feldmeyer et al. (2002, 2005)
L4e → L2/3i	1	10	Thomson et al. (2002) (rat)
	3	31	Thomson et al. (2002) (cat)
L4i → L2/3e	6	12	Thomson et al. (2002) (rat)

connection	existing	tested	publication
	10	37	Thomson et al. (2002) (cat)
L4e→L5e	12	86	Feldmeyer et al. (2005)*
L5e→L2/3e	1	29	Thomson et al. (2002)
	3	259	Thomson & Bannister (1998)

## Connectivity data analysis

To compare the connectivity maps we define recurrence strength as the ratio of the mean within-layer and the mean inter-layer connection probabilities and loop strength as the ratio of the mean connection probability of the cortical feed-forward loop (Gilbert (1983), L4 to L2/3 to L5 to L6 and back to L4) and the mean connection probability of all other inter-layer connections. For a fair comparison we base recurrence and loop strength only on connections for which estimates are available in both data sets. Therefore, layers 2/3, 4 and 5 are included but not layer 6.

A measure with higher resolution is the scaling factor  $\zeta$  which compares the connection probabilities of individual connections provided both connectivity maps assign non-zero probabilities.

$$\zeta = \frac{\max(C_a/\bar{C}_a, C_p/\bar{C}_p)}{\min(C_a/\bar{C}_a, C_p/\bar{C}_p)} \quad (8)$$

is independent of model size because  $C_m$  cancels from the expression (see *Supplemental Material*).

Furthermore, to quantify the specificity of connections we introduce the target specificity

$$T = \frac{C^{\text{post}=e} - C^{\text{post}=i}}{C^{\text{post}=e} + C^{\text{post}=i}}. \quad (9)$$

as the normalized difference of the connection probabilities constituting a projection.

## Consistent modifications of target specificity

In order to construct a consistent integrated connectivity map, it is necessary to modify the target specificity of certain projections (see *Results*), i.e. connection probabilities are modified to meet a given target specificity value. However, we constrain these modifications by demanding consistency with the underlying experimental data. For the anatomical data, this underlying measure is the number of synapses participating in a projection. For the physiological data, it is the measured connection probability of one of the two connections forming the projection (typically the second connection has not been quantified).

Modifying the connection probabilities while conserving the total number of synapses of a projection requires a redistribution of synapses across the target neurons (see supplementary Fig. 13). To that end, we determine the fraction of synapses targeting excitatory neurons  $\Delta$  as a function of the requested target specificity constrained by the total number of synapses and the sizes of the presynaptic and the two postsynaptic populations. The main complication is that target specificity is defined in terms of connection probabilities, see eq. (9), and the relation of connection probability and the number of synapses is non-linear, see

eq. (1) (for the exact expression see *Supplemental Material*). Nevertheless, in the first-order Taylor series expansion of  $C$ , eq. (2), the relation is linear and substituting  $C^{\text{post}=e} = \Delta K/(N^{\text{pre}} N^{\text{post}=e})$  and  $C^{\text{post}=i} = (1 - \Delta)K/(N^{\text{pre}} N^{\text{post}=i})$  in eq. (9) we find

$$\Delta = \frac{(1 + T)N^{\text{post}=e}}{(1 - T)N^{\text{post}=i} + (1 + T)N^{\text{post}=e}}.$$

The modifications of the physiological data are straightforward because in all cases considered here only one connection probability is experimentally given so that we can estimate the unknown value based on the definition eq. (9):

$$C^{\text{post}=i(e)} = \left( \frac{1 - T}{1 + T} \right)^{+(-1)} C^{\text{post}=e(i)}.$$

### Compilation of the integrated connectivity map

We compile the integrated connectivity map algorithmically. The procedure requires as input the anatomical and the physiological connectivity maps as well as the model size and information about desired modifications of the target specificities. The procedure automatically estimates the parameters of the Gaussian model and, based on these, the mean model connectivity. Subsequently the procedure separately modifies the target specificities of both scaled maps as instructed and finally averages the two maps (see also *Supplemental Material*).

### Layer-specific external input

We distinguish three types of layer-specific external inputs: thalamic afferents as reconstructed by Binzegger et al. (2004), “gray-matter” external inputs, i.e. intrinsic non-local inputs entering the local network through the gray matter, which we estimate based on the properties of axonal clusters (Binzegger et al., 2007), and “white-matter” external inputs, which include all inputs not covered by the previous types. The number of the latter is estimated based on the difference of the number of synapses the different cell types receive according to Binzegger et al. (2004) and the total synapse count in a given layer (Beaulieu & Colonnier, 1985).

The thalamic afferents are included in the anatomical connectivity map (Binzegger et al., 2004). We extract the gray-matter inputs from the information on bouton distributions in 3-dimensional space described in Binzegger et al. (2007). The authors find that boutons of all cell types form multiple clusters and the article provides the lateral distance of cluster centers and the corresponding somata. We interpret a cluster to be non-local if the lateral distance to the soma is larger than  $\approx 0.56$  mm (corresponding to a local network surface area of  $1 \text{ mm}^2$ ). By additionally using data on the relative sizes of different cluster types, we estimate the proportion of intrinsic gray-matter connections that originate outside of the local network. Thereupon, we use the estimated proportion of gray-matter inputs and the number of local connections in our network to calculate the absolute number of gray-matter inputs. In this way we construct an estimate of the gray-matter external inputs that is consistent with both, the axonal structure in Binzegger et al. (2007) and the structure of our model. The detailed procedure is described in the *Supplemental Material*.

The white-matter inputs are estimated based on the comparison of the absolute number of synapses obtained in Binzegger et al. (2004) which only contains

the contributions from local, thalamic and gray-matter synapses, with those in Beaulieu & Colonnier (1985) containing all synapses. The difference has been termed the “dark matter” of cortex (Binzegger et al., 2004) and, in case of the excitatory synapses, is usually interpreted as white-matter external inputs. The explicit numbers are published in Izhikevich & Edelman (2008, their figure 9 of the supplemental material) at subcellular resolution. As our model is based on point neurons, we sum over all contributions to a given cell type and average across the cell types that are collapsed to a single population in our model. Thereby, our estimates take neuronal morphology into account. The resulting counts for the three external input types as well as the total number of external inputs to the excitatory populations are given in supplementary Table 7. Since long-range projections target excitatory as well as inhibitory neurons (Johnson & Burkhalter, 1996; Gonchar & Burkhalter, 2003), we choose target specificity values for external inputs to be comparable to recurrent connections, resulting in similar total numbers of external inputs to inhibitory neurons (Table 3).

The cell-type specific external inputs are used as a reference parametrization of the model. To comprehensively assess the dependence of the activity on external inputs, we conduct simulations in which we choose the external inputs to a population randomly with uniform distribution: The inputs to the excitatory populations are constrained by the values from the reference and the layer-independent parametrization (compare supplementary Fig. 18). Those to inhibitory populations are chosen such that the target specificity of the external input to a given layer is between 0 and 0.1 (to L2/3, L4 and L5) and to L6, due to the high number of external inputs to excitatory cells in this layer, between 0 and 0.2.

## Network simulations

The network is defined by eight neuronal populations representing the excitatory and inhibitory cells in the four layers 2/3, 4, 5 and 6. The populations consist of current-based leaky integrate-and-fire model neurons with exponential synaptic currents (see *Supplemental Material*) and are randomly connected with connection probabilities according to the integrated connectivity map we derive in this article. Every population receives Poissonian background spike trains (Amit & Brunel, 1997; Brunel, 2000a); the firing rates of these inputs are composed by the number of external inputs a neuron in a particular population receives and the background spike rate contributed by each synapse. Synaptic strengths and synaptic time constants of all connections are chosen such that an average excitatory postsynaptic potential (EPSP) has an amplitude of 0.15 mV with a rise time of 1.6 ms and a width of 8.8 ms mimicking the *in vivo* situation (Fetz et al., 1991). Inhibitory strengths are negative and increased by a factor  $g$  compared to the excitatory ones. Delays in the network are chosen independent of the layer, with excitatory delays being on average around twice as long as inhibitory delays but the exact ratio is uncritical. To introduce heterogeneity into the network, we draw the synaptic strengths and delays from Gaussian distributions (prohibiting a change of sign of the strengths and constricting delays to be positive and multiples of the computation step size). The network structure and a complete list of parameters and their values for the reference network model are systematically described according to Nordlie et al. (2009) in Tables 2 and 3.

In some cases, we explicitly model the thalamic input to L4 and L6 by a thalamic population of 902 neurons (Peters & Payne, 1993) that emit Poissonian spike trains at a given rate in some prescribed time interval. These relay cells are ran-

A: Model summary					
<b>Populations</b>	nine; eight cortical populations and one thalamic population				
<b>Topology</b>	—				
<b>Connectivity</b>	random connections				
<b>Neuron model</b>	cortex: leaky integrate-and-fire, fixed voltage threshold, fixed absolute refractory period (voltage clamp), thalamus: fixed-rate Poisson				
<b>Synapse model</b>	exponential-shaped postsynaptic currents				
<b>Plasticity</b>	—				
<b>Input</b>	cortex: independent fixed-rate Poisson spike trains				
<b>Measurements</b>	spike activity, membrane potentials				
B: Populations					
Type	Elements	Number of populations	Population size		
Cortical network	iaf neurons	eight, two per layer	$N$ (type-specific)		
Th	Poisson	one	$N_{th}$		
C: Connectivity					
<b>Type</b>	random connections with independently chosen pre- and postsynaptic neurons; see <a href="#">Table 3</a> for probabilities				
<b>Weights</b>	fixed, drawn from Gaussian distribution				
<b>Delays</b>	fixed, drawn from Gaussian distribution multiples of sim. stepsize				
D: Neuron and synapse model					
<b>Name</b>	iaf neuron				
<b>Type</b>	leaky integrate-and-fire, exponential-shaped synaptic current inputs				
<b>Subthreshold dynamics</b>	$\frac{dV}{dt} = -\frac{V}{\tau_m} + \frac{I(t)}{C_m} \quad \text{if } (t > t^* + \tau_{ref})$ $V(t) = V_{\text{reset}} \quad \text{else}$ $I_{\text{syn}}(t) = w e^{-t/\tau_{\text{syn}}}$				
<b>Spiking</b>	If $V(t-) < \theta \wedge V(t+) \geq \theta$ 1. set $t^* = t$ , 2. emit spike with time stamp $t^*$				
E: Input					
Type	Target	Description			
Background	iaf neurons	independent Poisson spikes (see <a href="#">Table 3</a> )			
F: Measurements					
Spiking activity and membrane potentials from a subset of neurons in every population					

**Table 2:** Model description after [Nordlie et al. \(2009\)](#).

B+E: Populations and Inputs										
Name	L2/3e	L2/3i	L4e	L4i	L5e	L5i	L6e	L6i	Th	
Population size $N$	20683	5834	21915	5479	4850	1065	14395	2948	902	
External inputs $k_{\text{ext}}$	1600	1500	2100	1900	2000	1900	2900	2100	—	
Background rate $\nu_{\text{bg}}$	8 Hz									
C: Connectivity										
		from								
		L2/3e	L2/3i	L4e	L4i	L5e	L5i	L6e	L6i	Th
to	L2/3e	0.101	0.169	0.044	0.082	0.032	0.0	0.008	0.0	0.0
	L2/3i	0.135	0.137	0.032	0.052	0.075	0.0	0.004	0.0	0.0
	L4e	0.008	0.006	0.050	0.135	0.007	0.0003	0.045	0.0	0.0983
	L4i	0.069	0.003	0.079	0.160	0.003	0.0	0.106	0.0	0.0619
	L5e	0.100	0.062	0.051	0.006	0.083	0.373	0.020	0.0	0.0
	L5i	0.055	0.027	0.026	0.002	0.060	0.316	0.009	0.0	0.0
	L6e	0.016	0.007	0.021	0.017	0.057	0.020	0.040	0.225	0.0512
	L6i	0.036	0.001	0.003	0.001	0.028	0.008	0.066	0.144	0.0196
Name	Value	Description								
$w \pm \delta w$	$87.8 \pm 8.8 \text{ pA}$	excitatory synaptic strengths								
$g$	-4	relative inhibitory synaptic strength								
$d_e \pm \delta d_e$	$1.5 \pm 0.75 \text{ ms}$	excitatory synaptic transmission delays								
$d_i \pm \delta d_i$	$0.8 \pm 0.4 \text{ ms}$	inhibitory synaptic transmission delays								
D: Neuron Model										
Name	Value	Description								
$\tau_m$	10 ms	membrane time constant								
$\tau_{\text{ref}}$	2 ms	absolute refractory period								
$\tau_{\text{syn}}$	0.5 ms	postsynaptic current time constant								
$C_m$	250 pF	membrane capacity								
$V_{\text{reset}}$	-65 mV	reset potential								
$\theta$	-50 mV	fixed firing threshold								
$\nu_{\text{th}}$	15 Hz	thalamic firing rate during input period								

**Table 3:** Parameter specification. The categories refer to the model description in [Table 2](#).

domly connected to the cortex with the cell-type specific connection probabilities according to [Binzegger et al. \(2004\)](#), see [Table 3](#).

To instantiate the network model we randomly draw for every synapse the pre- and the postsynaptic neuron. In contrast to the often used convergent and divergent connectivity schemes ([Eppler et al., 2009](#)), this procedure results in binomially distributed numbers of incoming and outgoing synapses. In practice, we could first calculate the total number of synapses forming a connection by inverting [eq. \(1\)](#) and then successively create the synapses. In a distributed simulation setup, however, this procedure is inefficient because the neurons are distributed over multiple processes. Although a synapse is only created if the postsynaptic neuron is local to the process ([Morrison et al., 2005](#)) the full algorithm would have to be carried out on each process. We solve this problem by calculating *a priori* how many synapses will be created locally on each process, exploiting that the distribution of synapses over processes is multinomial. Subsequently we apply the serial algorithm on every machine to the local synapses only: The presynaptic neuron is drawn from all neurons in the presynaptic population and the postsynaptic cell on a given process is drawn only from the neurons located on this process (compare supplementary Fig. 16). While the first step is serial, but efficient for the number of processes we typically employ, the second step is fully parallelized. The procedure is detailed in the *Supplemental Material*. A reference implementation of this algorithm will be made available in the NEST simulation tool (<http://www.nest-initiative.org>) as `RandomPopulationConnect`.

All simulations are carried out with the NEST simulation tool ([Gewaltig & Diesmann, 2007](#)) using a grid constrained solver and a computation step size  $h = 0.1$  ms on a compute cluster with 24 nodes each equipped with 2 quad core AMD Opteron 2834 processors and interconnected by a 24 port Voltaire InfiniBand switch ISR9024D-M. 48 cores simulate the network of around 80,000 neurons and 0.3 billion synapses in close to real-time ([Djurfeldt et al., 2010](#)).

## Results

### Comparison of connectivity maps

The anatomical and the physiological connectivity maps exhibit a similar structure ([Fig. 2](#)): Recurrent within-layer connections are all non-zero with connection probabilities tending to decrease from superficial to deeper layers, excepting the physiological interneuron to interneuron connections which are, however, subject to poor statistics ([Table 1](#)). The inter-layer connections can be subdivided into connections with similar probabilities as within-layer connections and those with values close or equal to zero. Consequently, the recurrence strength, quantifying the relative strength of recurrent within-layer connections, is greater than one and statistically indistinguishable for the two maps (z-test,  $P > 0.1$ , [Fig. 2C](#)). Similarly, the loop strength, comparing the connectivity of the feed-forward loop to all other inter-layer connections, is indistinguishable (z-test,  $P > 0.05$ , [Fig. 2D](#)). However, 50% of the scaling factors of inter-layer connections are large (L2/3e to L4i, L5e to L2/3e, L4i to L2/3e and L4i to L2/3i) for both, the raw and the modified data.

### Lateral connectivity

In contrast to the largely consistent relative measures ([Fig. 2C and D](#)), absolute connection probability values differ (supplementary Table 6). We hypothesize that

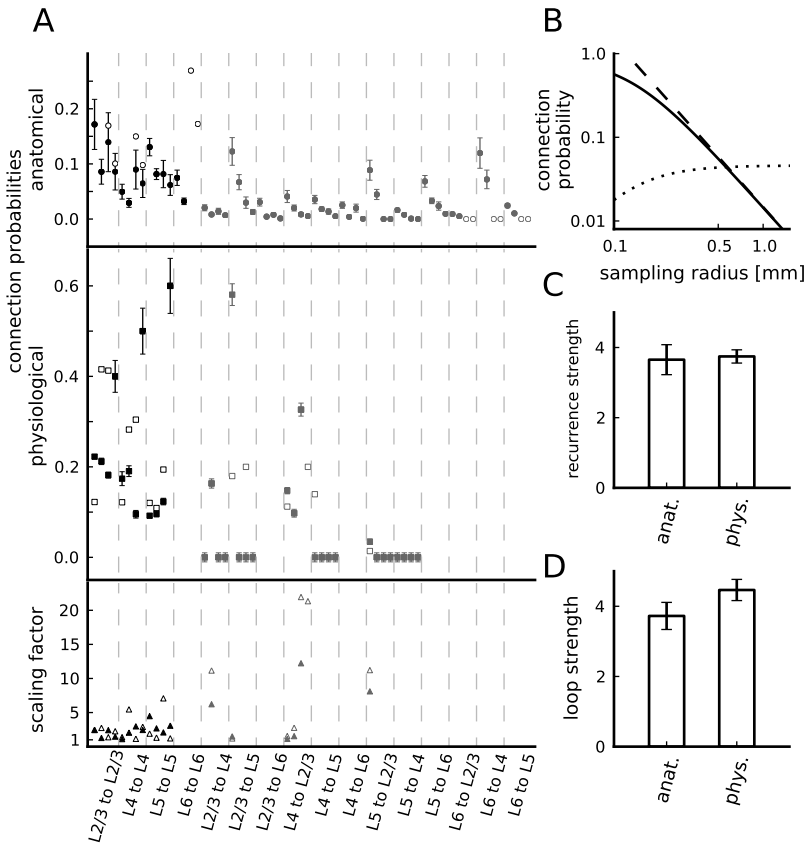


**Figure 2:** Properties of connectivity maps. (A) Connection probabilities according to the anatomical (top panel, circles) and physiological connectivity map (center panel, squares) and corresponding scaling factors (bottom panel, triangles). Both, raw (closed markers) and modified (open markers) are shown. The data are horizontally arranged according to their classification as within-layer (black) and inter-layer (gray) connections. For a given pair of pre- and post-synaptic layer, the data are arranged from left to right according to connection types: excitatory to excitatory, excitatory to inhibitory, inhibitory to excitatory and inhibitory to inhibitory. L5i to L5e/i outside of the displayed range, see supplementary Table 6. Error bars are minimal statistical errors (see *Supplemental Material*). (B) Sampling radius dependence of anatomical connection probability (solid: [eq. \(1\)](#), dashed: [eq. \(2\)](#)) and of the product of connection probability and area (dotted) in double-logarithmic representation. (C) Anatomical and physiological recurrence strength. (D) Anatomical and physiological loop strength. Error bars in C and D are based on the minimal statistical error estimates of connection probabilities using error propagation.

the differences in the mean connection probabilities are explained by differences in the methodology applied to obtain the connectivity maps: Physiological recordings in slices are usually restricted to a maximal lateral distance of the somata of around 100  $\mu\text{m}$  (as reported in [Thomson & Morris \(2002\)](#) for the raw physiological map). The anatomical data, in contrast, are based on reconstructed axons and dendrites, with axons extending up to 4mm ([Binzegger et al., 2007](#)), in general beyond 1mm. When providing absolute numbers, [Binzegger et al. \(2004\)](#) refer to the surface area of cat area 17 (399  $\text{mm}^2$ ).

We employ a Gaussian lateral connectivity model ([eq. \(4\)](#)), similar to the one by [Hellwig \(2000\)](#); [Buzas et al. \(2006\)](#) to account for the different experimental sampling radii (see *Materials and Methods*). We assume the model to reflect the *in vivo* connectivity structure and the experimental connectivity maps to characterize samples of this structure. The anatomical measurement is interpreted as an unconstrained sampling over the complete lateral connectivity structure while the physiological measurement corresponds to a local measure sampling from the center region of the Gaussian ([Fig. 3A](#)).

The model parameters, peak connection probability and lateral spread, are determined based on the mean connection probabilities of the two maps and the physiological sampling radius ([eqs. \(5\) and \(6\)](#), [Fig. 3](#)). The estimated lateral spread is consistent with data from rat and cat primary visual cortex based on the potential connectivity method: [Hellwig \(2000\)](#), caption to his figure 7, reports a lateral spread of 150 to 310  $\mu\text{m}$ , [Stepanyants et al. \(2008\)](#), their figure 7, find a spread of around 200  $\mu\text{m}$  of main projections in input and output maps. Also the overall connectivity level of 0.138 for nearby neurons with a distance of 100  $\mu\text{m}$  is in good agreement with the extensively used estimate of 0.1 provided by [Braitenberg & Schüz \(1998\)](#). These consistencies indicate that our underlying assumption –anatomical and physiological experiments sample independently from the same lateral connectivity profile– is valid.

**Average model connectivity** Our network model does not incorporate a lateral connectivity structure but randomly connected populations. We use the Gaussian lateral connectivity model exclusively to determine the average connection probability for a given network size ([eq. \(7\)](#), [Fig. 3D](#)). The connectivity of small networks (up to about 7,000 neurons) is largely determined by the physiological connectivity and the one of large networks (above 100,000 neurons) by the anatomical connection probability (decaying quadratically, see [Fig. 2B](#)). For intermediate network sizes, [eq. \(7\)](#) interpolates between these two extremes according to the Gaussian lateral connectivity profile. [Fig. 3E](#) shows the average synaptic convergence as a function of the network size. It reveals that only for large networks the majority of local synapses is represented in the model: for example a network of around 80,000 neurons comprises more than 85% of all local synapses. In contrast, a network of e.g. 10,000 neurons represents only around 20% of the local connectivity. Therefore, we select our network to correspond to 1  $\text{mm}^2$  of cortical surface (77,169 neurons).

According to our analysis the maximal average number of synapses per neuron is about 5,000. This number is consistent with the data of [Binzegger et al. \(2004\)](#), see their figure 11A). In [Fig. 3](#) we also display the connectivities and convergences of a selection of other modeling studies on the local cortical network (some data representing local networks embedded in larger networks). Independent of model size most studies use a connection probability around 0.1 which is largely consistent

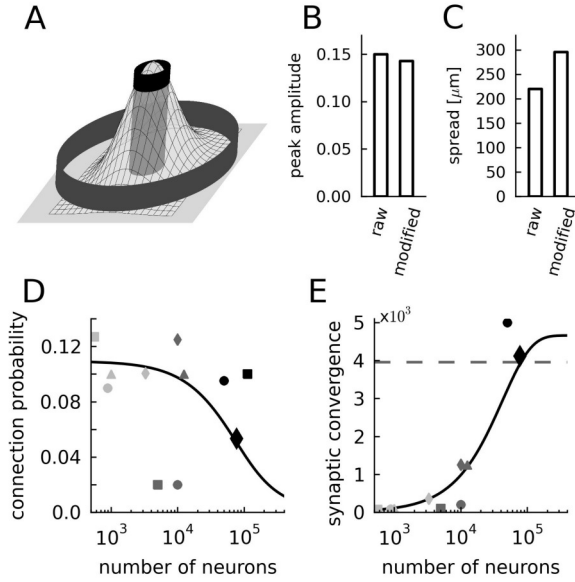


**Figure 3:** Lateral connectivity model. (A) Two dimensional Gaussian with two cylinders indicating the lateral sampling of the anatomical (gray outer cylinder) and the physiological (black inner cylinder) experiments. (B) Estimated peak amplitude and (C) lateral spread of the connectivity model based on mean connectivity of the anatomical and physiological raw and modified maps. (D) Average connection probability and (E) average synaptic convergence (average number of synaptic inputs per neuron) of the layered network model as a function of the network size expressed in number of neurons. The dashed horizontal line marks 85% of the maximal synaptic convergence in the local network. Black diamonds show the data used in our simulations, further markers indicate other published cortical network models: [Haeusler & Maass \(2007\)](#) (light gray square), [Izhikevich \(2006\)](#) (light gray triangle), [Izhikevich et al. \(2004\)](#) (light gray circle, embedded local network is defined by the area receiving connections from a single long-range axon), [Lundqvist et al. \(2006\)](#); [Djurfeldt et al. \(2008\)](#) (light gray diamond, local network represented by one hypercolumn), [Vogels & Abbott \(2005\)](#); [Vogels et al. \(2005\)](#) (dark gray circle), [Sussillo et al. \(2007\)](#) (dark gray square), [Brunel \(2000a\)](#) (dark gray triangle), [Kriener et al. \(2008\)](#) (dark gray diamond), [Kumar et al. \(2008\)](#) (black circles), [Morrison et al. \(2007\)](#) (black square).

with our results. Only for large networks of 50,000 neurons and more, this connection probability is above our estimate. Two studies use a significantly smaller connection probabilities of 0.02, arguing that this value interpolates between high local and low distal connectivity. Although the absolute numbers differ from our estimates, the reasoning is the same as for our model. In all but two cases (Morrison et al., 2007; Kumar et al., 2008) the models' convergence is maximally 20% of the anatomical estimate.

## Randomness and specificity

A central assumption of the anatomical connectivity map is randomness, i.e. synapses are established independent of the pre- and postsynaptic cell type. Nevertheless, the target specificity estimates of the anatomical connectivity map (circles in Fig. 4) are  $> 0.2$ , reflecting a preferential selection of excitatory targets. The bias is introduced by the application of Peters' rule, which assumes synaptic densities on dendrites to be independent of cell-type, to bouton densities and dendritic lengths. Furthermore, some projections exhibit very high values  $> 0.5$  because only the dendrites of excitatory cells, but barely those of inhibitory cells, reach into the cloud of presynaptic axonal elements.

The target specificity values of the physiological map contrast with the anatomical findings. Most values (squares in Fig. 4) are consistently smaller and show larger variability than the anatomical estimates. In addition, excitatory within-layer connections of the raw connectivity map univocally select their targets independent of the postsynaptic type. Several projections in the physiological map, however, connect exclusively to excitatory neurons due to incomplete sampling of inhibitory subtypes. This highlights that a straightforward application of the physiological connectivity map in simulations results in artifacts due to missing feed-forward inhibition. Finally, the projection from L2/3e to L4 specifically targets inhibitory, but not excitatory cells (see also Table 1).

The specific selection of inhibitory targets of the L2/3e to L4 projection cannot be explained by differences in the overlap of the excitatory and inhibitory dendrites with the excitatory axons and is therefore beyond the scope of anatomical studies relying on the statistics of neuronal morphology such as Peters' rule (Binzegger et al., 2004) and also potential connectivity (Stepanyants et al., 2008). The specificity in the inter-layer circuitry explains the large scaling factor of this projection (Fig. 2A).

We identify three additional candidates of specific target type selection: L5e to L2/3 (Dantzker & Callaway (2000); Thomson & Bannister (1998); Thomson et al. (2002); Lefort et al. (2009)) L2/3e to L6 (Zarinpar & Callaway, 2006) and L6e to L4 (McGuire et al., 1984), see *Supplemental Material* for details on the choice of these candidates. The structure of these projections has not been quantified comprehensively in paired recordings and evidence suggests that the target type selection is less strict than for the L2/3e to L4 projection. We tentatively assume them to have intermediate values (triangles in Fig. 4). Two of these projections (L2/3e to L4 and L5e to L2/3) are inverse to the feed-forward loop. Thomson & Morris (2002); Thomson et al. (2002) argued that the specific target type selection plays a distinct functional role because the inhibition-specific ("i-specific") feedback projections may prevent reverberant excitation involving L2/3, L4 and L5 and enhance the propagation of synchronous thalamic inputs.

We utilize the information on i-specific feedback and the anatomical estimates to remove for some projections the methodological biases by consistently mod-

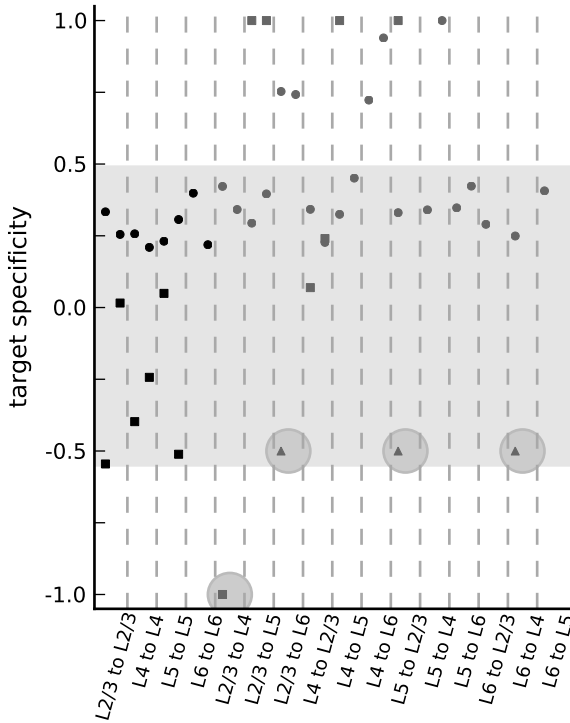


**Figure 4:** Anatomical (circles) and physiological (squares) target specificity estimates based on the modified connectivity maps.  $+1(-1)$  indicates exclusive selection of excitatory (inhibitory) targets, 0 random selection. Triangles show additional candidates of inhibition-specific projections discovered in photostimulation or electron microscopy studies. The shaded area highlights the estimates of within-layer projections and inter-layer projections with target specificity values between 0 and 0.5 (“non-specific” connections). Within these bounds the anatomical and physiological estimates are  $0.32 \pm 0.07$  and  $-0.17 \pm 0.28$ , respectively. The largest statistically well constrained values from a single laboratory are exhibited by the projections L2/3e to L2/3, L4e to L4 and L5e to L5 (compare supplementary Table 6) of the raw physiological map. The target specificity of these data is  $-0.01 \pm 0.03$ . The four highlighted data points are candidates of specific target type selection. For every pair pre- and post-synaptic layer the figure shows data both pre-synaptic neuron types (left: excitatory, right: inhibitory).

projection	$T$	data source
L2/3e to L4	-0.8	Thomson et al. 2002
L5e to L2/3	-0.4	Dantzker & Callaway 2000
L2/3e to L6	-0.4	Zarinpar & Callaway 2006
L6e to L4	-0.4	McGuire et al. 1984
L2/3e to L5	0.29	Binzegger et al. 2004
L4e to L5	0.32	Binzegger et al. 2004
L2/3i to L5	0.4	Binzegger et al. 2004
L4i to L2/3	0.23	Binzegger et al. 2004

**Table 4:** Amendment candidates for target specificity. The rows describe the projections whose target specificities are modified during the compilation of the integrated connectivity map. For each projection the second column states the target specificity value  $T$  after the amendment, the third the publication on which the modification is based. The top four rows are the candidate projections for a preference of inhibitory targets. In these cases, no quantitative estimates are known.  $T = -0.8$  is set if the literature provides a strong indication and  $T = -0.4$  for a comparably weak indication (compare *Supplemental Material*). The  $T$ -values of the bottom four rows are based on the anatomical map and provide estimates of the previously not measured connections to inhibitory neurons for the physiological map.

ifying the respective target specificities (see *Materials and Methods* and **Table 4**). Thereby, we estimate previously not measured physiological connection probabilities and introduce the specific selection of targets into the anatomical map. The latter constitutes an effective redistribution of synapses and corresponds to a refinement of Peter’s rule (supplementary Fig. 13).

### Integrated connectivity map

Based on the information gathered in the previous sections we now compile an integrated connectivity map. Our algorithmic compilation (see *Materials and Methods*) accounts for the differences in the lateral sampling of the two methods and corrects for methodological shortcomings expressed in the target specificity of projections (**Table 4**) by incorporating photostimulation and electron microscopy data.

The resulting connection probabilities are shown in the upper panel of **Fig. 5**. Visual inspection shows that the overall structure of the original connectivity maps is preserved. For a consistency check, we calculate the scaling factors between our integrated map and the recently published data for excitatory to excitatory connections of mouse C2 barrel column (Lefort et al., 2009). In this comparison we combine the data of Lefort et al. on L2 and L3 to L2/3 and on L5A and L5B to L5 according to eq. (3). The scaling factors (see **Fig. 5**, center panel) are low, indicating a good agreement of the connectivity maps. The main outlier is the recurrent L4e to L4e connection, which exhibits the highest connection probability in the study of Lefort et al. (2009) but rather low values in the physiological and especially the anatomical map. The lower panel of **Fig. 5** shows the target specificity values of the integrated connectivity map. Within-layer projections select their targets randomly and inter-layer projections inherit mostly the properties of the anatomical map, except for the four candidate i-specific projections.

The cell-type specific convergences and divergences (**Fig. 6**) show that the integrated connectivity map reflects prominent features of local cortical connectivity:

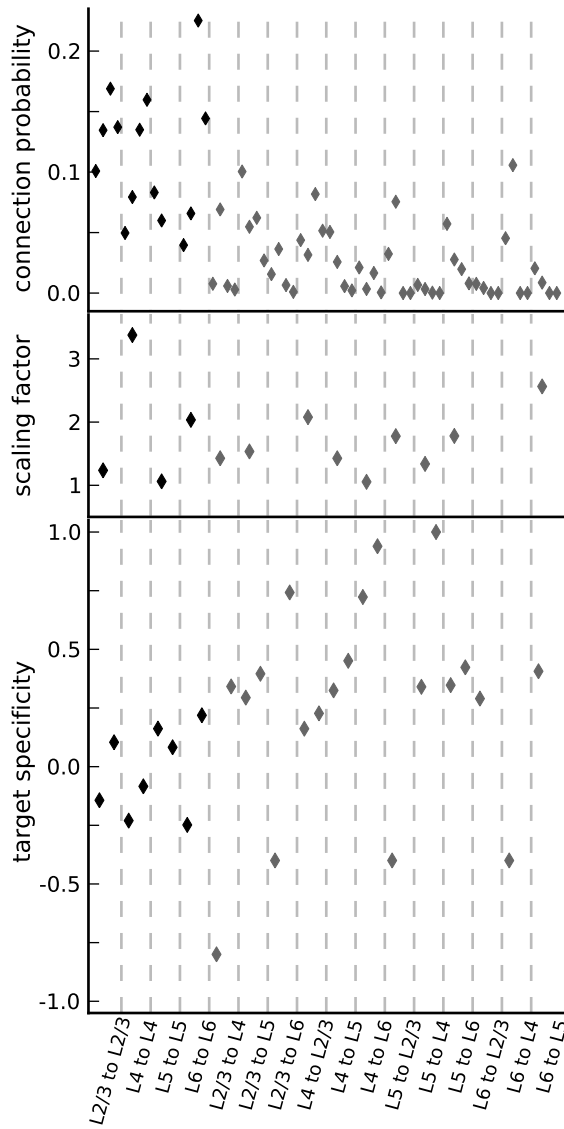


**Figure 5:** Properties of the integrated connectivity map. Layout of graphs as in Fig. 2 and Fig. 4 respectively. The top panel shows the connection probabilities of the model (L5i to L5e/i outside the displayed range, see Table 3). The center panel shows the scaling factors between the integrated map, restricted to excitatory to excitatory connections, and the recently published map of Lefort et al. (2009). The bottom panel shows the target specificity of the integrated connectivity map (within-layer connections:  $-0.02 \pm 0.17$ , non-specific inter-layer connections, see Fig. 4:  $0.33 \pm 0.08$ ).

Except for L5e, convergence is dominated by within-layer connections (consistent with e.g. [Douglas & Martin, 1991, 2004](#)). Furthermore, the strongest inter-layer excitatory to excitatory divergences correspond to the feed-forward loop from L4 to L2/3 to L5 to L6 and back to L4 ([Gilbert, 1983; Gilbert & Wiesel, 1983](#)). The excitatory to inhibitory divergence is dominated by the i-specific feedback connections.

By comparing the average convergence and divergence to the neuronal densities of the different cell populations (supplementary Fig. 14) we find that neurons in the local microcircuit sample most excitatory inputs from L2/3 and fewest from L5 and L6. In contrast, local outputs within the microcircuit project preferentially to L5.

**External inputs** The model consists in total of about 217 million excitatory and 82 million inhibitory synapses. The inhibitory synapse count is consistent with [Beaulieu & Colonnier \(1985\)](#) ( $64 \pm 21$  million) while the number of excitatory synapses is lower than their estimate ( $339 \pm 43$  million) presumably reflecting that a fraction of all excitatory synapses originates outside of the local network. The ratio of local synapses (total number of synapses in our network model) and all synapses (according to the countings of [Beaulieu & Colonnier \(1985\)](#)) is 0.74, similar to the ratio reported by [Binzegger et al. \(2004\)](#), but see [Stepanyants et al. \(2009\)](#).

The layer-specific external input structure distinguishes between thalamic afferents, gray-matter and white-matter inputs (see *Materials and Methods*). The resulting total number of external inputs per neuron ([Table 3](#)) is lowest in L2/3, intermediate in L4 and L5 and highest in L6. This relative structure is largely dominated by the white-matter inputs. In contrast, most gray-matter long-range inputs form synapses on L2/3 neurons and fewest form synapses in L6. Given the presently available data, we cannot exclude that some synapses treated here as external input actually represent a pathway in the local microcircuit still awaiting comprehensive experimental assessment.

### Spontaneous layer-specific activity

The simulated spontaneous spiking activity of all cell types corresponds to the asynchronous irregular activity state observed in mono-layered balanced random network models ([Amit & Brunel, 1997; Brunel, 2000a](#)). [Fig. 7](#) (A-D) shows the ongoing spontaneous spiking activity of all populations and the corresponding firing rates, irregularity and synchrony. The activity varies significantly across cell types. L2/3e and L6e exhibit the lowest firing rates with a mean below or close to 1 Hz. L4e cells fire more rapidly at around 4 Hz and L5e cells at more than 7 Hz. In all layers, inhibitory firing exceeds excitatory rates. The boxplots furthermore visualize that the firing rates of single neurons can differ substantially. For instance in L2/3e, several neurons fire at more than 5 Hz while the majority of neurons is rather quiescent emitting less than one spike per second. This effect is due to the binomially distributed convergence.

Single unit activity is irregular; the mean of the single unit coefficients of variation of the inter-spike intervals is greater than 0.8. The population activity is largely asynchronous, but exhibits fast oscillations with low amplitude similar to balanced random networks (e.g. [Brunel, 2000a](#)). We assess the synchrony of every population's multi-unit activity by the variability of the spike count histogram ([Fig. 7D](#)). At the given firing rates and bin width, the synchrony of the spiking

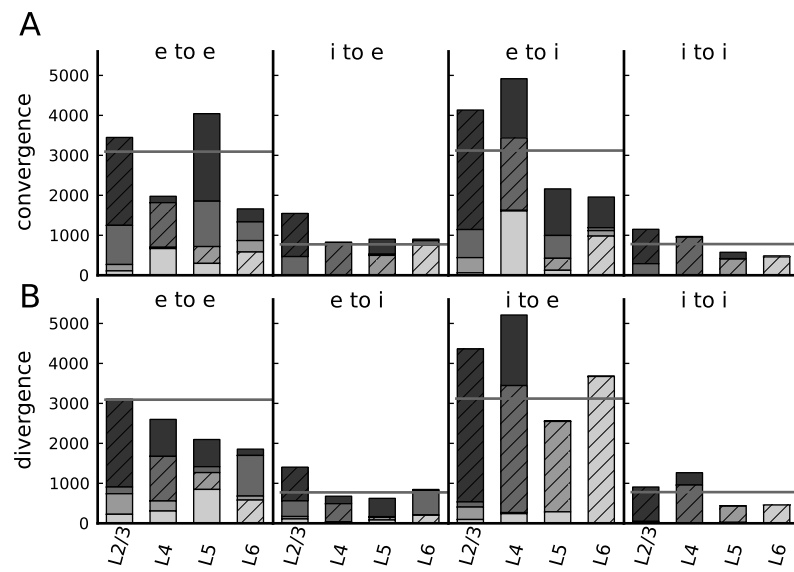


**Figure 6:** Cell-type specific convergence (A) and divergence (B) of the integrated connectivity map. The histograms display blocks of data for the four different connection types between excitatory (e) and inhibitory (i) neurons (as indicated). For a neuron in the layer specified on the horizontal axis, the individual bar segments show the absolute number of synapses the neuron receives from a source layer (convergence) or establishes in a target layer (divergence). Bar segments are arranged according to the physical location of the layers in the cortex (from top to bottom: L2/3, L4, L5, L6). Hatched bars represent within-layer connections. Lightness of gray increases from superficial to deeper layers. Gray horizontal lines indicate the convergence and divergence of a balanced random network with the same total number of neurons and synapses as the layered model.

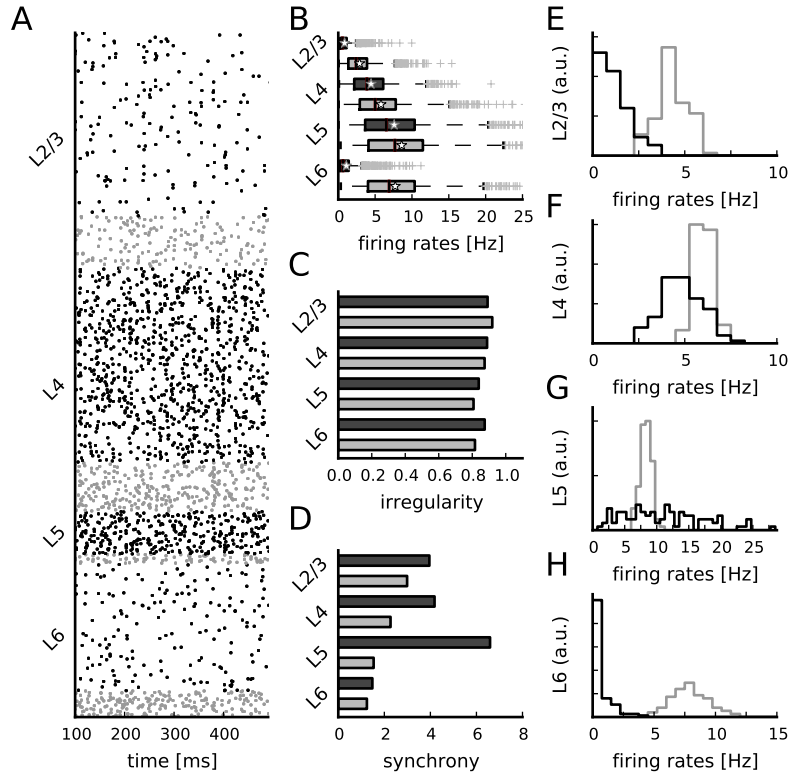


**Figure 7:** Spontaneous cell-type specific activity. (A) Raster plot of spiking activity recorded for 400 ms of biological time of layers 2/3, 4, 5 and 6 (from top to bottom; black: excitatory, gray: inhibitory). Relative number of displayed spike trains corresponds to the relative number of neurons in the network (total of 1862 shown). (B-D) Statistics of the spiking activity of all eight populations in the network based on 1000 spike trains recorded for 60 s (B and C) and 5 s (D) for every population. (B) Boxplot (Tukey, 1977) of single-unit firing rates. Crosses show outliers, stars indicate the mean firing rate of the population. (C) Irregularity of single-unit spike trains quantified by the coefficient of variation of the inter-spike intervals. (D) Synchrony of multi-unit spiking activity quantified by the variance of the spike count histogram (bin width 3 ms) divided by its mean. (E-H) Histograms of the excitatory and inhibitory population firing rates for L2/3 (E), L4 (F), L5 (G) and L6 (H) for randomly drawn external inputs (100 trials, see *Materials and Methods* for details).

activity is highest in L5e and lowest in L6. The synchrony of the membrane potential traces (Golomb, 2007, supplementary Fig. 20) confirms that the activity is asynchronous.

The observed activity features of the network do not depend on the specific structure of the external inputs: replacing the Poissonian background by a constant current (DC) to all neurons (supplementary Fig. 17) or applying layer-independent Poissonian background inputs (supplementary Fig. 18) yields similar results. Random selection of the number of external inputs (see *Materials and Methods*) also confirms the previous findings: Fig. 7 (E-H) shows the histograms of the population firing rates in the different layers for excitatory and inhibitory cells, respectively. The distribution of excitatory population firing rates in L2/3 and L6 are persistently low. L5e activity exhibits the highest firing rates and also the largest variability. L4e and the inhibitory populations vary only slightly with mean firing rates similar to the reference parametrization (Fig. 7B). Apparently, the local microcircuitry reconfigures the firing rate distributions for different input situations while conserving general features like the low rate regime in L2/3e and L6e. In 85% of the simulations, L2/3e and L6e fire at a lower rate than L4e and simultaneously L5e exhibits the highest firing rate. Also, we observe the inhibitory firing rate within a given layer to be higher than the excitatory rate in 83% of all cases.

**Comparison to in vivo activity** Table 5 contrasts the experimentally observed firing rates in individual layers with our simulation results. Experimentally, the spontaneous activity of L2/3e pyramids has been studied extensively. Consistent over species and areas the firing rate is below 1 Hz, in good quantitative agreement with the model. The L6e firing rates are similar to the model values, although the experimental data base is more sparse. The L4e and L5e firing rates of rat primary somato-sensory cortex are lower than in the model, but L5e consistently shows the highest spontaneous activity, also in rat auditory cortex. The activity of cortico-tectal cells in L5 (and L4) of various cortices in the rabbit is slightly higher. Several studies provide data on putative interneurons (Swadlow, 1988, 1989, 1991, 1994; Sakata & Harris, 2009), demonstrating that inhibitory activity is typically higher than that of excitatory cells. The statistics of single neuron spike trains in our model show great variations due to the random connectivity which also imposes a variance in the convergence of inputs. Therefore, “neighboring” neurons, i.e. neurons with statistically identical connectivity, can exhibit very different firing rates, which has also been observed experimentally (e.g. Swadlow, 1988; Heimel et al., 2005; de Kock & Sakmann, 2009).

**Stability of the network activity** The low-rate asynchronous irregular (AI) firing regime has been considered to be the ground state of cortical activity (Amit & Brunel, 1997). For the balanced random network model, the region of stability of the AI state is bounded by the relative strength of inhibitory synapses ( $> 4$ ) and sufficiently high background rates (Brunel, 2000a). Fig. 8 characterizes the AI state of the layered network. As in the balanced random network model, the layered network requires sufficient external input and sufficiently strong inhibitory coupling to enter the AI state. Increasing the background rate predominantly affects the activity of L4e, while an increase of the relative inhibitory synaptic strength decreases mostly the activity of L5e cells. Consequently, the order of excitatory firing rates (smallest in L2/3 and L6, highest in L5) is largely preserved except for large relative inhibitory synaptic strengths (combined with large background rates).

Species	Area	Firing rates [Hz]				data source
		L2/3e	L4e	L5e	L6e	
Mouse	S1	0.61	—	—	—	Crochet & Petersen (2006); Poulet & Petersen (2008)
Rat	V1	0.44	—	—	—	Greenberg et al. (2008)
Rat	M1	0.36	—	—	—	Lee et al. (2006)
Rat	S1	0.3	1.4	2-3	0.5	de Kock & Sakmann (2009)
Rat	A1	< 1	—	3-4	—	Sakata & Harris (2009)
Rabbit	4 areas	< 1	—	4-7	< 1	Swadlow (1988, 1989, 1991, 1994)
Squirrel	V1	0.19	0.35	1.7	0.74	Heimel et al. (2005)
Model	reference	0.86	4.45	7.59	1.09	Fig. 7B
Model	random	1.11 ± 0.8	4.8 ± 1.1	11 ± 6.1	0.56 ± 0.9	Fig. 7E-H

**Table 5:** Experimentally measured and simulated cell-type specific firing rates. Numerical columns show the layer-resolved mean firing rates obtained in *in vivo* awake animal recordings and in the present modeling study (last row indicates additionally the standard deviation). The investigated areas are S1: primary somato-sensory cortex, V1: primary visual cortex, M1: primary motor cortex, A1: primary auditory cortex. The four areas investigated in the rabbit by [Swadlow \(1988, 1989, 1991, 1994\)](#) are V1, S1, S2 (secondary somato-sensory cortex) and M1, respectively. In these four studies, L5 corresponds to cortico-tectal cells that are partly also located in L4. The data for the gray squirrel are the medians. The model results refer to the reference parametrization and to the mean ± std of the population rates for varying external inputs.

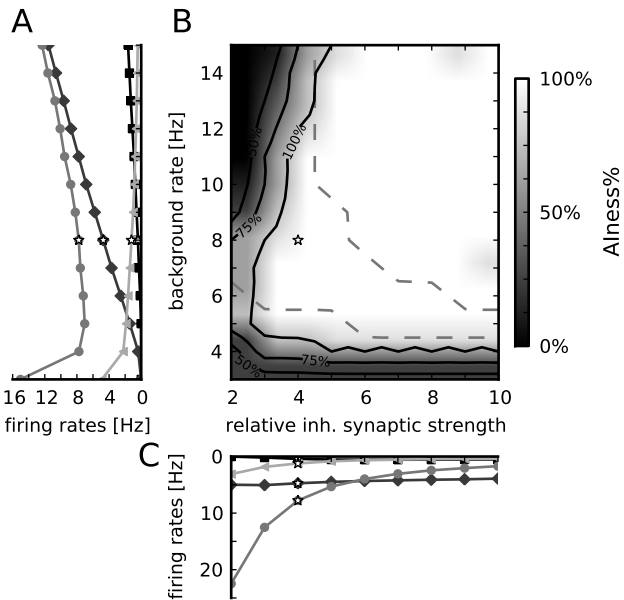


**Figure 8:** Dependence of network activity on the external background firing rate and the relative inhibitory synaptic strength. White stars mark the reference parameter set. (A) Population firing rates of excitatory populations in layers 2/3 (squares), 4 (diamonds), 5 (circles) and 6 (triangles), lightness increases with cortical depth, as a function of the background rate with fixed relative inhibitory synaptic strength (4). (B) Alness%, the percentage of populations with firing rate below 30 Hz, irregularity between 0.7 and 1.2, and synchrony below 8 (data collected for 5s per simulation), as a function of the background rate and the relative inhibitory synaptic strength. Labeled black iso-lines indicate areas where 50%, 75% and 100% of all populations fire asynchronously and irregularly at low rate. Dashed iso-lines confine the area where the firing rates are ordered in accordance to Table 5. (C) Population firing rates of excitatory populations as a function of the relative inhibitory synaptic strength at fixed background rate (8 Hz) (markers as in A).

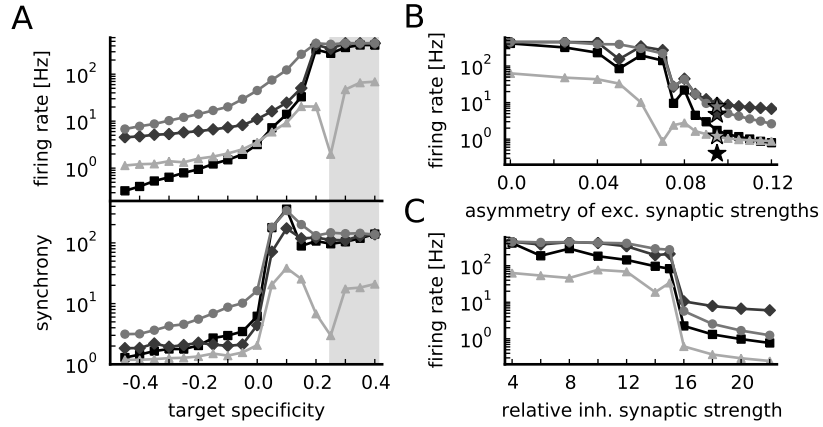


**Figure 9:** Relevance of target specificity for network stability. (A) Population firing rates (top panel) and synchrony (bottom panel), both in logarithmic representation, as a function of the target specificity of candidate projections L2/3e to L4 (negative values twice as large), L2/3e to L6, L5e to L2/3 and L6e to L4. A target specificity of 0 reflects random connectivity, gray-shaded area marks range of target specificity of other inter-layer connections ( $0.33 \pm 0.08$ ). (B) Population firing rates of the model with target specificity of candidate projections of +0.4 as a function of the asymmetry of excitatory to inhibitory and excitatory to excitatory synaptic strengths (defined as  $(w_{ie} - w_{ee})/(w_{ie} + w_{ee})$ , with fixed mean excitatory synaptic strength). Stars indicate firing rates of the reference model with target specificity of candidate projections of -0.4. (C) As B, but as a function of the relative inhibitory synaptic strength. All markers as in Fig. 8A.

**Role of i-specific projections for the stability of the AI state** In the following we conduct a series of simulation experiments where we alter the target type selection of the i-specific projections. The modifications affect exclusively the target specificity of these projections (upper four rows in Table 4). Technically, we compile for each parameter set a new connectivity map algorithmically (see *Materials and Methods*) so that the experimental data are fully respected. Fig. 9A shows that the firing rates and the synchrony of the excitatory populations first increase exponentially and then superexponentially when the target specificity of the four candidate projections approach random connectivity and then the level of other inter-layer connections, before the spike rates saturate for target specificity values above 0.2. The increase in synchronization precedes the firing rate increases. For L6e, we observe two outliers at  $T = 0.2$  and 0.25 where the activity in this layer corresponds to the low-rate AI state. This is likely due to the strong within-layer inhibitory feedback in L6 and the high amount of random external inputs to L6e. The general trend for L6 is nevertheless the same as for the other layers.

The modification of target specificity not only changes the local microcircuit at the level of specific cell types but also the overall level of excitation in the network. Therefore, we simulate further control networks which globally correct for the change in the level of excitation: we increase for all connections, not only for the i-specific candidates, the synaptic strength of excitatory to inhibitory connections and simultaneously reduce the synaptic strength of excitatory to excitatory connections. Fig. 9B shows that a sufficiently large asymmetry of excitatory synaptic strengths with respect to target cell type counterbalances the overexcitation. However, the natural order of the excitatory activity levels of the cortical layers

([Table 5](#)) is partly inverted.

This stabilization procedure uses different excitatory synaptic strengths according to the target cell type and thereby introduces an additional parameter. Therefore, we also investigate whether the network can alternatively be stabilized by changing an already existing parameter, the relative inhibitory synaptic strength. We find that only implausibly large values ( $> 15$ ) lead to a stable low-rate AI state ([Fig. 9C](#)) and that also in this case the order of firing rates is partly inverted.

In summary, a layered network model that is parametrized equivalent to the balanced random network model requires the inclusion of i-specific feedback connections in order to exhibit asynchronous irregular spiking activity. The alternative stabilization of the network by global changes of parameters results in a distribution of layer-specific firing rates in conflict with experimental observations.

### Propagation of transient thalamic inputs

Confronted with a transient thalamic input the layered network model responds with a stereotypic propagation of activity through the different layers. [Fig. 10A](#) shows an exemplary spike raster of the model after a short-lasting increase of thalamic firing rate. The cell-type specific activity pattern is consistent over 100 different network and input instantiations ([Fig. 10B](#)).

**Amplitude and timing of cell-type specific responses** L2/3e, L4e and L5e emit a comparable amount of additional spikes in response to the stimulus while L6e shows a comparatively sparse response ([Fig. 10B](#)). In total, only a minority of all neurons in the network is activated by the thalamic stimulus ([Fig. 10E](#)). Only in L5e a large fraction of all cells emits additional spikes in response to the stimulus. In relation to the ongoing activity, we find that the input layers (L4 and L6) exhibit a similar dynamical gain which is much lower than the gain of the output layers L5 and especially L2/3.

The response is initiated in the input layers and then propagates to layers L2/3 and L5 (see [Fig. 10A, B](#)). The latency of activation (defined as the maximum of the excitatory spike count histogram) is shortest in L4 followed by L6 and L5, and finally L2/3. The early onset of activation of L5, not after but rather synchronously with L2/3, is in contrast to the expectation according to the classical notion of the feed-forward loop from L4 to L2/3 to L5 ([Gilbert, 1983](#)) but in agreement with the experimental activity data ([Sakata & Harris, 2009](#), compare also [Mitzdorf, 1985](#)). The feed-forward connection from L2/3 to L5 causes the prolonged response in L5 that is reflected in the second peak in the spike count. L6, being already slightly excited by the thalamic input, receives feed-forward input from L5 which triggers a sparse response during the ramp-up phase in L5. The activity is back to baseline in all layers before the last thalamic spikes arrive at cortex. Deactivation is ordered similar to activation, starting in L4, followed by L2/3 and L6, and finally L5.

**Interplay of excitation and inhibition in the propagation of inputs** Not only the excitatory populations but also the inhibitory populations show a distinct activation pattern (see [Fig. 10A](#), gray dots, and [B](#), gray lines). Initially, as the interneurons in any layer receive the same, albeit slightly weaker, feed-forward inputs, the inhibitory response resembles the excitatory response. However, the inhibitory populations show, in contrast to the respective excitatory populations, two pronounced activation peaks in L2/3, L4 and L6. As shown above, these

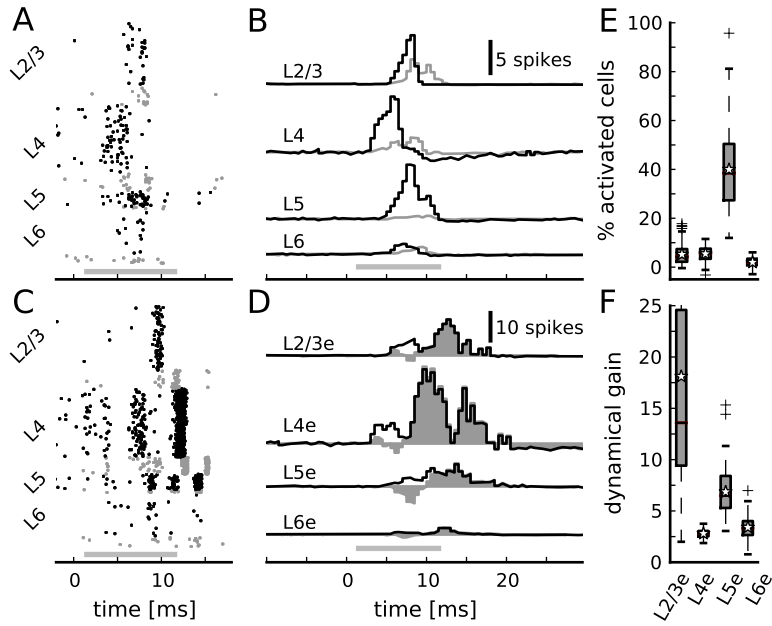


**Figure 10:** Response to transient thalamic input. Thalamic firing rates increase step-like by 15 Hz for a duration of 10 ms; 0 ms corresponds to the onset of transient input, gray bars show the arrival of thalamic spikes at cortical neurons taking the mean delay (for simplicity the same as within the network, 1.5 ms) into account. (A) Cell-type specific spiking activity of the network with i-specific projections. Markers as in Fig. 7A. (B) Corresponding cell-type specific population spike counts averaged over 100 instantiations of network and input (excitatory populations in black, inhibitory in gray). Spike counts are calculated with a bin-width of 0.5 ms with the number of recorded neurons L3e: 500, L3i: 141, L4e: 529, L4i: 132, L5e: 117, L5i: 25, L6e: 347, L6i: 71 (numbers correspond to relative population sizes). (C) Spiking activity of a control network without i-specific projections (target specificity of candidate projections of +0.4) stabilized by an asymmetry of excitatory synaptic strengths of 0.095. (D) Corresponding cell-type specific population spike counts of excitatory populations averaged over 100 instantiations. Filled area shows the difference of the data in D and B. (E) Average percentage of cells in the excitatory populations that are activated by thalamic stimulation in relation to the ongoing activity (according to the data in B). (F) Dynamical gain, defined as the firing rate during the stimulus presentation divided by the spontaneous firing rate, of excitatory populations (according to data in B).

layers receive i-specific feedback connections. Apparently, the cell-type specific connectivity structure results in a complex interplay of excitation and inhibition not explained by within-layer recurrent inhibition and thereby shapes the propagating response to a transient thalamic input. Specifically we observe that the activation of L2/3 entails the increased activity of inhibitory interneurons in L4, thereby stopping the excitatory activity in this layer. A similar effect is observed in the next step of the feed-forward loop between L2/3 and L5. Activation of L2/3 prolongs the excitatory activity in L5 as stated above. In contrast, the early activation of L5 results in a sharpening of the response in L2/3 by the additional activation of L2/3 interneurons. The connection from L6e to L4i adds to the sharpening of the L4 response and the rather weak i-specific connection from L2/3 to L6 plays a role in preventing a stronger ramp-up of excitatory activity in L6.

### Role of i-specific feedback connections for the propagation of inputs

These observations suggest that the i-specific feedback connections control the duration and the amplitude of the response to thalamic inputs. To further elucidate their role for the propagation of input-related activity, we study the response of a network without i-specific feedback connections but similar spontaneous activity. The small differences in the firing rates (compare Fig. 9B) are reflected in the initial response of the network to the thalamic input (first bumps in the spike count histograms in Fig. 11D) which exhibits a steeper increase in L2/3e and L4e and is weaker in L5e. After this initial phase, the response is drastically different and shows reverberating activation of the different layers lingering well beyond the offset of the input. The response is much stronger and shows oscillatory components by reciprocal activation of the different layers. The effect stays the same, albeit smaller, for a control network with the candidate projections having a target specificity value of +0.2 which is well below the range for non-specific inter-layer connections.

## Discussion

### Modeling approach

The present work extends the balanced random network model (Amit & Brunel, 1997; Brunel, 2000a; van Vreeswijk & Sompolinsky, 1996, 1998) to multiple layers with realistic connection probabilities. Despite their reduced structure the mono-layered models exhibit qualitatively consistent activity dynamics and the classical analysis of them has guided our research. Our neuron and synapse model as well as the random connectivity scheme do not differ qualitatively from the earlier work. The model size is selected sufficiently large to incorporate the majority of all local synapses. The network structure, one excitatory and one inhibitory population in each layer, represents the minimal laminar extension of the mono-layered models and also the minimal set of cell types typically distinguished in experiments. Data resolving the connectivity at a finer scale (e.g. Mercer et al., 2005; West et al., 2006) are combined to match the more coarse resolution of our model. Previous multi-layered models partly use the same approach (e.g. Haeusler et al., 2009) and partly more detailed cell type classifications (e.g. Traub et al., 2005; Izhikevich & Edelman, 2008). However, quantitative connectivity data are not yet widely and consistently available on a finer level of detail so that it remains unclear which dynamical consequences any further separation of cell types implies.

## Integrated connectivity map

The success of the dynamical analysis in the second part of the study relies on our finding that the two connectivity maps are consistent when one considers the differences in methodology. The compiled connectivity map accounts for these, but it nevertheless mingles data not only from multiple laboratories but also from different cortical areas and species. This choice is not exclusively motivated by canonicity in structure (e.g. [Douglas et al., 1989](#); [Nelson, 2002](#); [Groh et al., 2010](#)) and activity ([Table 5](#)), but driven by the incompleteness of data for a specific area and species. The density of neurons in our model is based on cat area 17 and the density of synapses is consistent with cat data ([Beaulieu & Colonnier, 1985](#)). The most crucial difference between our map and the original data based maps is the target specific structure which removes the fundamental bias introduced by undersampling of inhibitory cells (electrophysiology) or by the application of Peters' rule (anatomy).

The integrated connectivity map is consistent with the most prominent features of the cortical microcircuit: the recurrence of connections ([Douglas & Martin, 1991](#)) and the feed-forward loop from L4 to L2/3 to L5 to L6 to L4 ([Gilbert, 1983](#)). The excitatory sub-circuit is largely consistent with the recently published excitatory map of the C2 barrel column of the mouse ([Lefort et al., 2009](#)). In addition, the circuit exhibits a distinct feedback structure with projections targeting predominantly interneurons from L2/3e to L4 and from L5e to L2/3. [Thomson et al. \(2002\)](#); [Thomson & Morris \(2002\)](#) recognized the potential of selective feedback projections for stabilizing the activity and increasing the sensitivity for time-dependent signaling, but were not able to test this hypothesis. Furthermore, reports on the projections from L6e to L4 and the rather weak projection from L2/3e to L6 indicate specific selection of inhibitory target cells. Our selection of the projection from L6e to L4 is based on the electron microscopy study by [McGuire et al. \(1984\)](#), providing sparse and partial data. In their discussion, [Ahmed et al. \(1994\)](#) present an alternative interpretation of these data proposing that many synapses originally assigned to inhibitory targets are potentially on excitatory cells. Still they acknowledge that the relative number of synapses targeting interneurons is very high in comparison to other excitatory projections. The ongoing discussion on this projection has recently been reviewed by [Thomson \(2010\)](#).

Here, we quantified the dynamical relevance of these i-specific connections for spontaneous and evoked activity. Especially the two feedback projections (L2/3e to L4 and L5e to L2/3) are crucial for stability and reliable input propagation because of the relatively small structural and dynamical impact of L6 on other layers. Extending the idea of i-specific feedback, it is a conceivable but untested hypothesis that L6e (especially cortico-thalamic cells) targets predominantly interneurons in L5, too.

## Model parametrization

Only a subset of the required model parameters are known experimentally. Here, we focus on cell-type specific structural parameters: the numbers of neurons, the numbers of external inputs and the connection probabilities between neurons. Other parameters like neuronal parameters, synaptic strengths and delays are selected independent of the cell type. This choice enables us to expose the dynamical consequences of the structure of the local microcircuit unaffected by additional cell-type specificity (e.g. [Brémaud et al., 2007](#); [Lefort et al., 2009](#)). The consistency

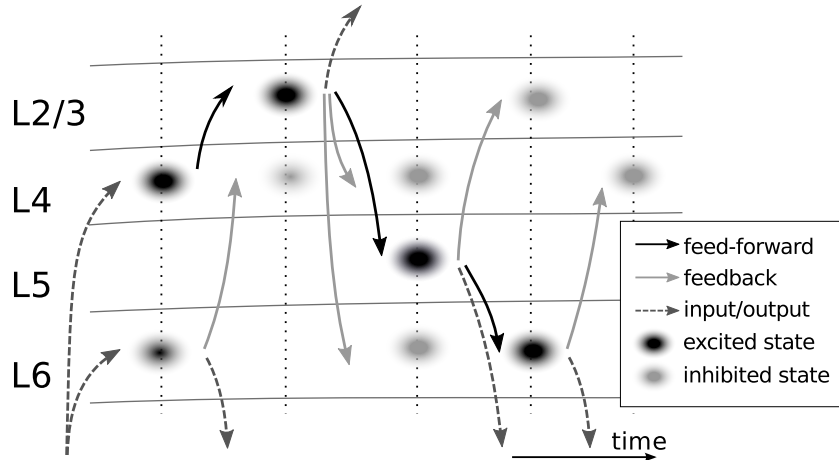


**Figure 11:** Sketch of the flow of activity following transient thalamic input. Black and gray ellipses represent excited and inhibited activity states, respectively. Dark gray dashed arrows indicate input and output of the local network. The black arrows represent the feed-forward loop projections L4 to L2/3 to L5 to L6. The gray arrows correspond to the activation of the candidate i-specific connections (L2/3e to L4 and to L6, L5e to L2/3 and L6e to L4).

of the activity in our model with the experimental data suggests that the (static) connectivity structure plays a dominant role in shaping the neuronal activity and that it is not required to model complex neuronal features such as morphology to reproduce the experimental findings discussed here. In future, modeling of more complex neuronal dynamics will eventually reveal where spatially extended neuron models are required to understand the experimentally observed phenomena.

An exception to the cell-type independent parametrization is the increased synaptic strength for the connection from L4e to L2/3e. Although this change affects the ongoing activity only marginally (supplementary Fig. 19), it is important for a successful transmission of activity from L4 to L2/3 following thalamic stimulation. The modification is motivated by the large discrepancies of the L4i to L2/3 projection in the anatomical and physiological maps and the difference in the relative convergence of excitatory inputs from L2/3 and L4 to L2/3 pyramids between our model and [Feldmeyer et al. \(2006\)](#). To ultimately resolve this issue, it might be necessary to incorporate additional specificity ([Yoshimura et al., 2005](#); [Sarid et al., 2007](#); [Fares & Stepnyants, 2009](#)) and, despite a plethora of studies on the L4 to L2/3 connections, potentially additional experiments especially regarding the inhibitory projection.

### Cell-type specific activity

The application of the integrated connectivity map and the parametrization according to balanced random network models ([Brunel, 2000a](#)) results in asynchronous irregular activity without specific tuning. This activity state is stable over a wide range of parameters regarding e.g. external inputs, synaptic strengths and delays.

The model predicts cell-type specific firing rates in agreement with data from awake animals ([Table 5](#)). In particular, the connectivity map captures the low excitatory firing rates in L2/3 and L6 quantitatively although mono-layered models hardly show stable activity at these low levels of activity ([Sussillo et al., 2007](#)). The particular ordering of firing rates depends, however, on the inclusion of i-specific

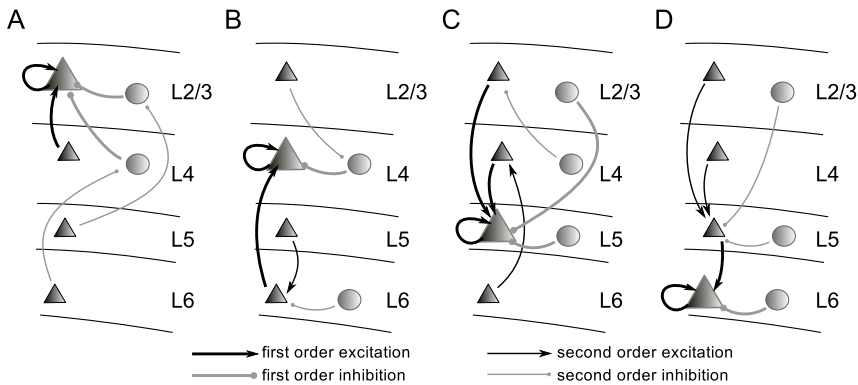


**Figure 12:** Differences in input structure for the excitatory cell types L2/3e (A), L4e (B), L5e (C) and L6e (D) (large triangles). The illustrations show the strongest pathways of direct (first-order, thick arrows) and indirect (second-order, thin arrows) excitation (black) and inhibition (gray) of a given population (see *Supplemental Material* for further details). Triangles represent excitatory and circles inhibitory populations.

feedback connections. The lacking consistency of the firing rates in previous models is presumably due to the incompleteness of the previously used connectivity maps.

Confronted with a transient thalamic input, the model shows a concise propagation of activity from the input layers to the output layers (compare [Miller, 1996](#)). The propagation pattern (Fig. 11) is shaped by the interaction of excitation and inhibition between the different layers and promotes a temporal neural code ([Thomson & Morris, 2002](#)).

### Relation of structure and activity

The differences in the cell-type specific input structure (Fig. 12) shed light on the mechanisms underlying the observed activity features. For example, the low firing rates of L2/3e and L6e neurons have different structural origins: L2/3e effectively integrates, next to the excitatory inputs from L2/3e and L4e, inhibitory inputs from all layers. In contrast, L6e interacts largely with the recurrent within-L6 network; other inputs predominantly pass through L5e and rather modulate L6e activity. L4e is also dominated by within-layer connectivity and the i-specific inputs from L2/3 and L6 modulate its activity and temporally structure the response to transient stimuli. L5 consists of relatively few neurons and correspondingly forms rather few recurrent within-layer inputs. Furthermore, L5e integrates the highest number of first-order inputs, but does not receive i-specific projections. As a result, L5e reacts with a wide range of firing rates to changes in the external input, especially in comparison to the other layers. This, together with the control that L5 exerts on L2/3 by the i-specific feedback, puts it in a special position to integrate and amplify information. Inhibitory cells receive predominantly excitatory inter-layer inputs (supplementary Fig. 15) and therefore exhibit elevated firing rates.

### Conclusion

The connectivity structure of the local cortical network shapes the cell-type specific activity and defines functional roles of the different layers. Any fine-scale connectivity structure (e.g. [Song et al., 2005](#); [Yoshimura et al., 2005](#); [Kampa et al., 2006](#))

faces the constraints imposed by the connectivity implemented in this model. The presented framework can be continuously refined as new data become available and extends the available mathematical methods to infer synaptic connectivity from neuronal morphology. Based on the currently available data it reproduces prominent activity features, suggesting that these arise predominantly from the network structure, not single cell properties. The results predict distinct activity patterns of interneurons and highlight the need to uncover the target specificity of projections in future experiments.

**Acknowledgements:** We are grateful to Kathleen S. Rockland and Dirk Feldmeyer for fruitful discussions about the structure of the local cortical network, and to our colleagues in the NEST Initiative for continued support. We also acknowledge Ad Aertsen for his contributions in the initial phase of the project. Partially supported by the Helmholtz Alliance on Systems Biology, EU Grant 15879 (FACETS), EU Grant 269921 (BrainScaleS), DIP F1.2, BMBF Grant 01GQ0420 to BCCN Freiburg, and the Next-Generation Supercomputer Project of MEXT (Japan).

## References

Ahmed, B., Anderson, J., Douglas, R., Martin, K., & Nelson, J. (1994). Polyneuronal innervation of spiny stellate neurons in cat visual cortex. *J. Compar. Neurol.* 341(1), 39–49.

Ali, A. B., Bannister, A. P., & Thomson, A. M. (2007). Robust correlations between action potential duration and the properties of synaptic connections in layer4 interneurones in neocortical slices from juvenile rats and adult rat and cat. *J. Physiol. (Lond.)* 580(1), 149–169.

Amit, D. J., & Brunel, N. (1997). Model of global spontaneous activity and local structured activity during delay periods in the cerebral cortex. *Cereb. Cortex* 7, 237–252.

Bannister, A. P., & Thomson, A. M. (2007). Dynamic properties of excitatory synaptic connections involving layer 4 pyramidal cells in adult rat and cat neocortex. *Cereb. Cortex* 17(9), 2190–2203.

Barbour, D. L., & Callaway, E. M. (2008). Excitatory local connections of superficial neurons in rat auditory cortex. *J. Neurosci.* 28(44), 11174–11185.

Beaulieu, C., & Colonnier, M. (1983). The number of neurons in the different laminae of the binocular and monocular regions of area 17 in the cat. *J. Compar. Neurol.* 217, 337–344.

Beaulieu, C., & Colonnier, M. (1985). A laminar analysis of the number of round-asymmetrical and flat-symmetrical synapses on spines, dendritic trunks, and cell bodies in area 17 of the cat. *J. Compar. Neurol.* 231, 180–189.

Beierlein, M., & Connors, B. W. (2002). Short-term dynamics of thalamocortical and intracortical synapses onto layer 6 neurons in neocortex. *J. Neurophysiol.* 88, 1924–1932.

Beierlein, M., Gibson, J. R., & Connors, B. W. (2003). Two dynamically distinct inhibitory networks in layer 4 of the neocortex. *J. Neurophysiol.* 90, 2987–3000.

Binzegger, T., Douglas, R. J., & Martin, K. A. C. (2004). A quantitative map of the circuit of cat primary visual cortex. *J. Neurosci.* 39(24), 8441–8453.

Binzegger, T., Douglas, R. J., & Martin, K. A. C. (2007). Stereotypical bouton clustering of individual neurons in cat primary visual cortex. *J. Neurosci.* 27(45), 12242–12254.

Binzegger, T., Douglas, R. J., & Martin, K. A. C. (2009). Topology and dynamics of the canonical circuit of cat V1. *Neural Networks* 22(8), 1071–1078.

Braitenberg, V., & Schüz, A. (1998). *Cortex: Statistics and Geometry of Neuronal Connectivity* (2nd ed.). Berlin: Springer-Verlag.

Brémaud, A., West, D. C., & Thomson, A. M. (2007). Binomial parameters differ across neocortical layers and with different classes of connections in adult rat and cat neocortex. *Proc. Nat. Acad. Sci. USA* 104(35), 14134–14139.

Briggs, F. (2010). Organizing principles of cortical layer 6. *Frontiers in Neural Circuits* 4(3). doi: 10.3389/neuro.04.003.2010.

Brunel, N. (2000a). Dynamics of sparsely connected networks of excitatory and inhibitory spiking neurons. *J. Comput. Neurosci.* 8(3), 183–208.

Brunel, N. (2000b). Dynamics of sparsely connected networks of excitatory and inhibitory spiking neurons. *J. Comput. Neurosci.* 8(3), 183–208.

Buzas, P., Kovacs, K., Ferecsko, A. S. Budd, J. M. L., & Eysel, U. T. Kisvarday, Z. F. (2006). Model-based analysis of excitatory lateral connections in the visual cortex. *J. Compar. Neurol.* 499, 861–881.

Crochet, S., & Petersen, C. C. H. (2006). Correlating whisker behavior with membrane potential in barrel cortex of awake mice. *Nat. Neurosci.* 9(5), 608–610.

Dantzker, J. L., & Callaway, E. M. (2000). Laminar sources of synaptic input to cortical inhibitory interneurons and pyramidal neurons. *Nat. Neurosci.* 3(7), 701–707.

Davis, C. S. (1993). The computer generation of multinomial random variates. *Computational Statistics & Data Analysis* 16, 205–217.

de Kock, C. P. J., & Sakmann, B. (2009). Spiking in primary somatosensory cortex during natural whisking in awake head-restrained rats is cell-type specific. *Proc. Natl. Acad. Sci. USA* 106(38), 16446–16450.

Djurfeldt, M., Hjorth, J., Eppler, J. M., Dudani, N., Helias, M., Potjans, T. C., Bhalla, U. S., Diesmann, M., Hellgren Kotaleski, J., & Ekeberg, Ö. (2010). Runtime interoperability between neuronal network simulators based on the MUSIC framework. *Neuroinformatics* 8, 43–60.

Djurfeldt, M., Lundqvist, M., Johansson, C., Rehn, M., Ekeberg, O., & Lansner, A. (2008). Brain-scale simulation of the neocortex on the IBM Blue Gene/L supercomputer. *IBM Journal of Research and Development* 52(1/2), 31–41.

Douglas, R., & Martin, K. (2007a). Mapping the matrix: the ways to neocortex. *Neuron* 56, 226–238.

Douglas, R. J., Martin, K. A., & Whitteridge, D. (1989). A canonical microcircuit for neocortex. *Neural Comput.* 1, 480–488.

Douglas, R. J., & Martin, K. A. C. (1991). A functional microcircuit for cat visual cortex. *J. Physiol. (Lond)* 440, 735–769.

Douglas, R. J., & Martin, K. A. C. (2004). Neuronal circuits of the neocortex. *Annu. Rev. Neurosci.* 27, 419–451.

Douglas, R. J., & Martin, K. A. C. (2007b). The butterfly and the loom. *Brain Res. Bull.* 55, 314–328.

Elhanany, E., & White, E. L. (1990). Intrinsic circuitry: synapses involving the local axon collaterals of corticocortical projection neurons in the mouse primary somatosensory cortex. *J. Compar. Neurol.* 291, 43–54.

Eppler, J. M., Helias, M., Muller, E., Diesmann, M., & Gewaltig, M. (2009). PyNEST: a convenient interface to the NEST simulator. *Front. Neuroinform.* 2, 12.

Fares, T., & Stepanyants, A. (2009). Cooperative synapse formation in the neocortex. *Proc. Natl. Acad. Sci. USA* 106(38), 16463–16468.

Feldmeyer, D., Lübke, J., & Sakmann, B. (2006). Efficacy and connectivity of intracolumnar pairs of layer 2/3 pyramidal cells in the barrel cortex of juvenile rats. *J. Physiol. (Lond.)* 575, 583–602.

Feldmeyer, D., Lübke, J., Silver, R. A., & Sakmann, B. (2002). Synaptic connections between layer 4 spiny neurone-layer 2/3 pyramidal cell pairs in juvenile rat barrel cortex: physiology and anatomy of interlaminar signalling within a cortical column. *J. Physiol. (Lond.)* 538(3), 803–822.

Feldmeyer, D., Roth, A., & Sakmann, B. (2005). Monosynaptic connections between pairs of spiny stellate cells in layer 4 and pyramidal cells in layer 5a indicate that lemniscal and paralemniscal afferent pathways converge in the infragranular somatosensory cortex. *J. Neurosci.* 25(13), 3423–3431.

Fetz, E., Toyama, K., & Smith, W. (1991). Synaptic interactions between cortical neurons. In A. Peters (Ed.), *Cerebral Cortex*, Volume 9, Chapter 1, pp. 1–47. New York and London: Plenum Press.

Gabbott, P. L., & Somogyi, P. (1986). Quantitative distribution of GABA-immunoreactive neurons in the visual cortex (area 17) of the cat. *Exp. Brain Res.* 61(2), 323–331.

Gewaltig, M.-O., & Diesmann, M. (2007). NEST (Neural Simulation Tool). *Scholarpedia* 2(4), 1430.

Gilbert, C. D. (1983). Microcircuitry of the visual cortex. *Annu. Rev. Neurosci.* 6, 217–247.

Gilbert, C. D., & Wiesel, T. N. (1983). Clustered intrinsic connections in cat visual cortex. *J. Neurosci.* 5, 1116–33.

Golomb, D. (2007). Neuronal synchrony measures. *Scholarpedia* 2(1), 1347.

Gonchar, Y., & Burkhalter, A. (2003). Distinct GABAergic targets of feedforward and feedback connections between lower and higher areas of rat visual cortex. *J. Neurosci.* 23(34), 10904–10912.

Greenberg, D. S., Houweling, A. R., & Kerr, J. N. D. (2008). Population imaging of ongoing neuronal activity in the visual cortex of awake rats. *Nat. Neurosci.* 11(7), 749–751.

Groh, A., Meyer, H. S., Schmidt, E. F., Heintz, N., Sakmann, B., & Krieger, P. (2010). Cell-type specific properties of pyramidal neurons in neocortex underlying a layout that is modifiable depending on the cortical area. *Cereb. Cortex* 20(4), 826–836.

Haeusler, S., & Maass, W. (2007). A statistical analysis of information-processing properties of lamina-specific cortical microcircuit models. *Cereb Cortex* 17(1), 149–162.

Haeusler, S., Schuch, K., & Maass, W. (2009). Motif distribution, dynamical properties, and computational performance of two data-based cortical microcircuit templates. *J. Physiol. (Paris)* 103(1–2), 73–87.

Heimel, J. A., Van Hooser, S. D., & Nelson, S. B. (2005). Laminar organization of response properties in primary visual cortex of the gray squirrel (*sciurus carolinensis*). *J. Neurophysiol.* 94, 3538–3554.

Heinze, J., Hepp, K., & Martin, K. A. C. (2007). A microcircuit model of the frontal eye fields. *J. Neurosci.* 27(35), 9341–9353.

Hellwig, B. (2000). A quantitative analysis of the local connectivity between pyramidal neurons in layers 2/3 of the rat visual cortex. *Biol. Cybern.* 2(82), 111–121.

Hill, S., & Tononi, G. (2005). Modeling sleep and wakefulness in the thalamocortical system. *J Neurophysiol* 93(3), 1671–1698. Comparative Study.

Holmgren, C., Harkany, T., Svennenfors, B., & Zilberter, Y. (2003). Pyramidal cell communication within local networks in layer 2/3 of rat neocortex. *J. Physiol. (Lond.)* 1(551), 139–153.

Izhikevich, E. M. (2006). Polychronization: Computation with spikes. *Neural Comput.* 18, 245–282.

Izhikevich, E. M., & Edelman, G. M. (2008). Large-scale model of mammalian thalamocortical systems. *Proc. Natl. Acad. Sci. USA* 105(9), 3593–3598.

Izhikevich, E. M., Gally, J. A., & Edelman, G. M. (2004). Spike-timing dynamics of neuronal groups. *Cereb. Cortex* 14, 933–944.

Johnson, R. R., & Burkhalter, A. (1996). Microcircuitry of forward and feedback connections within rat visual cortex. *J. Compar. Neurol.* 368, 383–398.

Kampa, B. M., Letzkus, J. J., & Stuart, G. J. (2006). Cortical feed-forward networks for binding different streams of sensory information. *Nat. Neurosci.* 9(12), 1472–1473.

Kapfer, C., Glickfeld, L., Atallah, B., & Scanziani, M. (2007). Supralinear increase of recurrent inhibition during sparse activity in the somatosensory cortex. *Nat. Neurosci.* 10(6), 743–753.

Kriener, B., Tetzlaff, T., Aertsen, A., Diesmann, M., & Rotter, S. (2008). Correlations and population dynamics in cortical networks. *Neural Comput.* 20, 2185–2226.

Kumar, A., Schrader, S., Aertsen, A., & Rotter, S. (2008). The high-conductance state of cortical networks. *Neural Comput.* 20(1), 1–43.

Le Be, J.-V., & Markram, H. (2006). Spontaneous and evoked synaptic rewiring in the neonatal neocortex. *Proc. Natl. Acad. Sci. USA* 103(35), 13214–13219.

Lee, A., Manns, I., Sakmann, B., & Brecht, M. (2006). Whole-cell recordings in freely moving rats. *Neuron* 51, 399–407.

Lefort, S., Tomm, C., Sarria, J.-C. F., & Petersen, C. C. H. (2009). The excitatory neuronal network of the C2 barrel column in mouse primary somatosensory cortex. *Neuron* 61, 301–316.

Lundqvist, M., Rehn, M., Djurfeldt, M., & Lansner, A. (2006). Attractor dynamics in a modular network model of neocortex. *Network: Comput. Neural Systems* 17(3), 253–276.

Maffei, A., Nelson, S. B., & Turrigiano, G. G. (2004). Selective reconfiguration of layer 4 visual circuitry by visual deprivation. *Nat. Neurosci.* 7(12), 1353–1359.

Markram, H., Lübke, J., Frotscher, M., Roth, A., & Sakmann, B. (1997). Physiology and anatomy of synaptic connections between thick tufted pyramidal neurons in the developing rat neocortex. *J. Physiol. (Lond)* 500(2), 409–440.

Martin, K. A. C., & Whitteridge, D. (1984). Form, function, and intracortical projections of spiny neurons in the striate visual cortex of the cat. *J. Physiol. (Lond.)* 353, 463–504.

Mason, A., Nicoll, A., & Stratford, K. (1991). Synaptic transmission between individual pyramidal neurons of the rat visual cortex in vitro. *J. Neurosci.* 11(1), 72–84.

McGuire, B. A., Hornung, J.-P., Gilbert, C. D., & Wiesel, T. N. (1984). Patterns of synaptic input to layer 4 of cat striate cortex. *J. Neurosci.* 4(12), 3021–3033.

Mercer, A., West, D. C., Morris, O. T., Kirchhecker, S., Kerkhoff, J. E., & Thomson, A. M. (2005). Excitatory connections made by presynaptic cortico-cortical pyramidal cells in layer 6 of the neocortex. *Cereb. Cortex* 15, 1485–1496.

Miller, R. (1996). Neural assemblies and laminar interactions in the cerebral cortex. *Biol. Cybern.* 75(3), 253–261.

Mitzdorf, U. (1985). Current source-density method and application in cat cerebral cortex: Investigation of evoked potentials and eeg phenomena. *Physiol. Rev.* 65(1), 37–100.

Morrison, A., Aertsen, A., & Diesmann, M. (2007). Spike-timing dependent plasticity in balanced random networks. *Neural Comput.* 19, 1437–1467.

Morrison, A., Mehring, C., Geisel, T., Aertsen, A., & Diesmann, M. (2005). Advancing the boundaries of high connectivity network simulation with distributed computing. *Neural Comput.* 17(8), 1776–1801.

Nelson, S. B. (2002). Cortical microcircuits: Diverse or canonical? *Neuron* 36, 19–27.

Nordlie, E., Gewaltig, M.-O., & Plesser, H. E. (2009). Towards reproducible descriptions of neuronal network models. *PLoS Comput Biol* 5(8), e1000456.

Peters, A., & Payne, B. R. (1993). Numerical relationships between geniculocortical afferents and pyramidal cell modules in cat primary visual cortex. *Cereb. Cortex* 3(1), 69–78.

Poulet, J., & Petersen, C. (2008). Internal brain state regulates membrane potential synchrony in barrel cortex of behaving mice. *Nature* 454(7206), 881–5.

Ren, M., Yoshimura, Y., Takada, N., Horibe, S., & Komatsu, Y. (2007). Specialized inhibitory synaptic actions between nearby neocortical pyramidal neurons. *Science* 316, 758–761.

Sakata, S., & Harris, K. D. (2009). Laminar structure of spontaneous and sensory-evoked population activity in auditory cortex. *Neuron* 64, 404–418.

Sarid, L., Bruno, R., Sakmann, B., Segev, I., & Feldmeyer, D. (2007). Modeling a layer 4-to-layer 2/3 module of a single column in rat neocortex: Interweaving in vitro and in vivo experimental observations. *Proc. Natl. Acad. Sci. USA* 104(41), 16353–16358.

Schubert, D., Kötter, R., Luhmann, H. J., & Staiger, J. F. (2006). Morphology, electrophysiology and functional input connectivity of pyramidal neurons characterizes a genuine layer va in the primary somatosensory cortex. *Cereb. Cortex* 16, 223–236.

Silberberg, G., & Markram, H. (2007). Disynaptic inhibition between neocortical pyramidal cells mediated by martinotti cells. *Neuron* 53, 735–746.

Song, S., Per, S., Reigl, M., Nelson, S., & Chklovskii, D. (2005). Highly nonrandom features of synaptic connectivity in local cortical circuits. *Public Library of Science, Biology* 3(3), 0507–0519.

Stepanyants, A., Hirsch, J., Martinez, L. M., Kisvarday, Z. F., Ferecsko, A. S., & Chklovskii, D. B. (2008). Local potential connectivity in cat primary visual cortex. *Cereb. Cortex* 18(1), 13–28.

Stepanyants, A., Martinez, L. M., Ferecskó, A. S., & Kisvárday, Z. F. (2009). The fractions of short- and long-range connections in the visual cortex. *Proc. Natl. Acad. Sci. USA* 106(9), 3555–3560.

Sussillo, D., Toyoizumi, T., & Maass, W. (2007). Self-tuning of neural circuits through short-term synaptic plasticity. *J. Neurophysiol.* 97, 4079–4095.

Swadlow, H. A. (1988). Efferent neurons and suspected interneurons in binocular visual cortex of the awake rabbit: Receptive fields and binocular properties. *J. Neurophysiol.* 59(4), 1162–1187.

Swadlow, H. A. (1989). Efferent neurons and suspected interneurons in s-1 vibrissa cortex of the awake rabbit: Receptive fields and axonal properties. *J. Neurophysiol.* 62(1), 288–308.

Swadlow, H. A. (1991). Efferent neurons and suspected interneurons in second somatosensory cortex of the awake rabbit: Receptive fields and axonal properties. *J. Neurophysiol.* 66(4), 1392–1409.

Swadlow, H. A. (1994). Efferent neurons and suspected interneurons in motor cortex of the awake rabbit: Axonal properties, sensory receptive fields, and subthreshold synaptic inputs. *J. Neurophysiol.* 71(2), 437–453.

Thomson, A. M. (1997). Activity-dependent properties of synaptic transmission at two classes of connections made by rat neocortical pyramidal axons in vitro. *J. Physiol. (Lond.)* 502(1), 131–147.

Thomson, A. M. (2010). Neocortical layer 6, a review. *Frontiers in Neuroanatomy* 4(13). doi: 10.3389/fnana.2010.00013.

Thomson, A. M., & Bannister, A. P. (1998). Postsynaptic pyramidal target selection by descending layer iii pyramidal axons: dual intracellular recordings and biocytin filling in slices of rat neocortex. *Neuroscience* 84(3), 669–683.

Thomson, A. M., Bannister, A. P., Mercer, A., & Morris, O. T. (2002). Target and temporal pattern selection at neocortical synapses. *Philosophical Transactions of the Royal Society London, Series B* 357, 1781–1791.

Thomson, A. M., & Deuchars, J. (1997). Synaptic interactions in neocortical local circuits: Dual intracellular recordings in vitro. *Cereb. Cortex* 7, 510–522.

Thomson, A. M., & Lamy, C. (2007). Functional maps of neocortical local circuitry. *Frontiers in Neuroscience* 1(1), 19–42.

Thomson, A. M., & Morris, O. T. (2002). Selectivity in the inter-laminar connections made by neocortical neurones. *J. Neurocytol.* 31, 239–246.

Thomson, A. M., West, D. C., & Deuchars, J. (1995). Properties of single axon excitatory postsynaptic potentials elicited in spiny interneurons by action potentials in pyramidal neurons in slices of rat neocortex. *Neuroscience* 69(3), 727–738.

Thomson, A. M., West, D. C., Hahn, J., & Deuchars, J. (1996). Single axon ipsp's elicited in pyramidal cells by three classes of interneurons in slices of rat neocortex. *J. Physiol. (Lond.)* 496(1), 81–102.

Thomson, A. M., West, D. C., Wang, Y., & Bannister, A. (2002). Synaptic connections and small circuits involving excitatory and inhibitory neurons in layer 2-5 of adult rat and cat neocortex: Triple intracellular recordings and biocytin labelling in vitro. *Cereb. Cortex* 12, 936–953.

Traub, R. D., Contreras, D., Cunningham, M. O., Murray, H., LeBeau, F. E. N., Roopun, A., Bibbig, A., Wilent, W. B., Higley, M. J., & Whittington, M. A. (2005). Single-column thalamocortical network model exhibiting gamma oscillations, sleep spindles, and epileptogenic bursts. *J Neurophysiol* 93(4), 2194–2232. Comparative Study.

Tukey, J. W. (1977). *Exploratory data analysis*. Addison-Wesley.

van Vreeswijk, C., & Sompolinsky, H. (1996). Chaos in neuronal networks with balanced excitatory and inhibitory activity. *Science* 274, 1724–1726.

van Vreeswijk, C., & Sompolinsky, H. (1998). Chaotic balanced state in a model of cortical circuits. *Neural Comput.* 10, 1321–1371.

Vogels, T. P., & Abbott, L. F. (2005). Signal propagation and logic gating in networks of integrate-and-fire neurons. *J. Neurosci.* 25(46), 10786–10795.

Vogels, T. P., Rajan, K., & Abbott, L. F. (2005). Neural network dynamics. *Annu. Rev. Neurosci.* 28, 357–376.

Wang, Y., Markram, H., Goodman, P. H., Berger, T. K., Ma, J., & Goldman-Rakic, P. S. (2006). Heterogeneity in the pyramidal network of the medial prefrontal cortex. *Nat. Neurosci.* 9(4), 534–542.

West, D. C., Mercer, A., Kirchhecker, S., Morris, O. T., & Thomson, A. M. (2006). Layer 6 cortico-thalamic pyramidal cells preferentially innervate interneurons and generate facilitating epsps. *Cereb. Cortex* 16, 200–211.

White, E. L., & Keller, A. (1987). Intrinsic circuitry involving the local axon collaterals of corticothalamic projection cells in mouse smi cortex. *J. Compar. Neurol.* 262, 13–26.

Yoshimura, Y., Dantzker, J., & Callaway, E. (2005). Excitatory cortical neurons form fine-scale functional networks. *Nature* 433(24), 868–873.

Zarrinpar, A., & Callaway, E. M. (2006). Local connections to specific types of layer 6 neurons in the rat visual cortex. *J. Neurophysiol.* 95, 1751–1761.

## Supplemental Material

### Connection probabilities

**Derivation of Eq. (1)** The connection probability  $C_{N^{\text{pre}},N^{\text{post}}}(K)$  of two neurons from populations of sizes  $N^{\text{pre}}$  and  $N^{\text{post}}$  which are randomly connected (with uniform probability) by  $K$  synapses can be derived as follows: the probability that a particular pair of neurons is connected is equal to one minus the probability that it is not connected, i.e.

$$C_{N^{\text{pre}},N^{\text{post}}}(K) = 1 - q_{N^{\text{pre}},N^{\text{post}}}(K).$$

Since the  $K$  synapses are created independently,  $q_{N^{\text{pre}},N^{\text{post}}}(K)$  is the probability of not being connected by any of the synapses

$$q_{N^{\text{pre}},N^{\text{post}}}(K) = \prod_{i=1}^K q_{N^{\text{pre}},N^{\text{post}}}(1) = [q_{N^{\text{pre}},N^{\text{post}}}(1)]^K.$$

The probability of not being connected by a particular synapse is one minus the probability of being so

$$\begin{aligned} q_{N^{\text{pre}},N^{\text{post}}}(1) &= 1 - C_{N^{\text{pre}},N^{\text{post}}}(1) \\ &= 1 - 1/N^{\text{pre}}N^{\text{post}}, \end{aligned}$$

hence

$$C_{N^{\text{pre}},N^{\text{post}}}(K) = 1 - \left(1 - \frac{1}{N^{\text{pre}}N^{\text{post}}}\right)^K.$$

**Taylor-series expansion of Eq. (1)** The expression for the connection probability can be expanded in a Taylor series using the binomial series

$$(1+x)^K = 1 + Kx + \frac{K(K-1)}{2}x^2 + \dots$$

Although conversion is guaranteed for  $x < 1$ , we require  $K^2x^2 \rightarrow 0$  in order to write  $(1+x)^K = 1 + Kx$ . With  $x = -1/N^{\text{pre}}N^{\text{post}}$  we find the approximation

$$\begin{aligned} C_{N^{\text{pre}},N^{\text{post}}}(K) &= 1 - \left(1 - \frac{1}{N^{\text{pre}}N^{\text{post}}}\right)^K \\ &= 1 - (1+x)^K \\ &= 1 - (1+Kx) \\ &= -Kx \\ &= \frac{K}{N^{\text{pre}}N^{\text{post}}} \end{aligned}$$

valid for small  $K/N^{\text{pre}}N^{\text{post}}$ .

**Errors of experimental connection probabilities** A lower bound for the statistical error of  $C_a$  results from the experimental standard deviations of the neuron count by [Beaulieu & Colonnier \(1983\)](#) and the consideration of error propagation.

The physiological search for connected neurons corresponds to a random sampling test, so that the statistical error of the number of connected neuron pairs

$\delta(RQ)$  is given by the standard deviation of the binomial distribution. Therefore, the statistical error of the connection probability is  $\delta C_p = \sqrt{C_p(1 - C_p)/Q}$  (given  $Q > 0$ ). For untested connections (i. e.  $\sum_j Q_j = 0$ ), we set  $\delta C_p = 0.01$ .

Both estimates are minimal statistical errors. The estimate for the anatomical data ignores errors in the estimation of the number of synapses as well as errors due to the limited number of reconstructed axons and dendrites. Both error estimates do not account for any potential systematic error e.g. due to sampling biases. The minimal statistical errors are sufficient to show that recurrence strength and loop strength of the two connectivity maps (see Fig. 2) are statistically indistinguishable.

### Gaussian lateral connectivity model

The anatomical and physiological mean connection probabilities  $C_{a/p}$  correspond to the integration of the lateral connectivity profile  $C(r)$  over the corresponding sampling radius  $r_{a/p}$ , i.e.  $C_{a/p} = 1/(\pi r_{a/p}^2) \int_0^{r_{a/p}} \int_0^{2\pi} C(r) r dr d\varphi$ , yielding the two equations

$$C_a = 2\pi C_0 \sigma^2 / (\pi r_a^2) [1 - \exp(-r_a^2/2\sigma^2)] \quad (10)$$

$$C_p = 2\pi C_0 \sigma^2 / (\pi r_p^2) [1 - \exp(-r_p^2/2\sigma^2)]. \quad (11)$$

Assuming that the parameters of the lateral connectivity profile  $C_0$  and  $\sigma$  are identical in both equations, we find

$$\frac{\pi r_a^2 C_a}{1 - \exp(-r_a^2/2\sigma^2)} = \frac{\pi r_p^2 C_p}{1 - \exp(-r_p^2/2\sigma^2)}.$$

This equation can be solved numerically for  $\sigma$ . For  $r_a \gg \sigma$  we have  $\exp(-r_a^2/2\sigma^2) = 0$  and therefore

$$\exp(-r_p^2/2\sigma^2) = 1 - \frac{\pi r_p^2 C_p}{\pi r_a^2 C_a}$$

which can be solved for  $\sigma$ :

$$\sigma = r_p \left[ -2 \ln \left( 1 - \frac{\pi r_p^2 C_p}{\pi r_a^2 C_a} \right) \right]^{-1/2}.$$

$C_0$  can now be found by solving eq. (10) (or analogously eq. (11)):

$$C_0 = \frac{\pi r_a^2 C_a}{2\pi\sigma^2} \left[ 1 - \exp \left( -\frac{r_a^2}{2\sigma^2} \right) \right]^{-1}.$$

In practice, we are interested in the limit  $r_a \rightarrow \infty$ , arriving at eq. (5) for  $\sigma$  and, using  $\lim_{r_a \rightarrow \infty} \exp(-r_a^2/2\sigma^2) = 0$ , eq. (6) for  $C_0$ .

The resulting parameters depend on the sampling radius of the physiological experiments, i.e. the lateral distance of the somata of cells in the paired recordings. For the raw data set, this value is provided (100  $\mu\text{m}$ , [Thomson & Morris, 2002](#)). The modified physiological map, however, combines different experiments with potentially different sampling radii. Here, we find that increasing the sampling radius increases the zero-distance connection probability monotonically but decreases the lateral spread. Nevertheless, the effect is small: the estimates of both parameters change by less than 8% when altering the sampling radius from 50 to 150  $\mu\text{m}$ .

## Scaling factor

The scaling factor  $\zeta$  is used to compare measurements of connection probabilities of individual connections. In order to first remove global differences that arise from the differences in the lateral sampling, we scale the connection probabilities  $C_{a/p}$  of a connectivity map such that the new mean of the map corresponds to a previously determined model connectivity  $C_m$ :  $C'_{a/p} \leftarrow C_{a/p} C_m / \bar{C}_{a/p}$ , where  $\bar{C}_{a/p}$  denotes the global mean of the original connectivity map. The ratio of the scaled individual connection probabilities is 1 if two maps differ with respect to the lateral sampling but are otherwise in perfect agreement. In order to exclusively measure the quality of the agreement, we remove the information which connectivity map provides the larger estimate by calculating the ratio of the larger of the two estimates divided by the smaller one

$$\zeta = \frac{\max(C'_a, C'_p)}{\min(C'_a, C'_p)} \quad \text{if } C'_{a/p} > 0,$$

restricting the measure to  $\zeta > 1$ . Instead of scaling to a previously determined model connectivity, it is equivalent to compare the normalized connection probabilities

$$\begin{aligned} \zeta &= \frac{\max(C'_a, C'_p)}{\min(C'_a, C'_p)} \\ &= \frac{\max(C_a C_m / \bar{C}_a, C_p C_m / \bar{C}_p)}{\min(C_a C_m / \bar{C}_a, C_p C_m / \bar{C}_p)} \\ &= \frac{\max(C_a / \bar{C}_a, C_p / \bar{C}_p)}{\min(C_a / \bar{C}_a, C_p / \bar{C}_p)}. \end{aligned}$$

This can be seen by substituting the mathematical definitions of  $\max(x, y)$  and  $\min(x, y)$ ,  $|x + y| \pm |x - y|$ .

## Consistent modification of target specificity: exact expression for redistribution of synapses

The redistribution of synapses is a method to modify the connection probabilities forming a projection while conserving the total number of synapses. The connection probability is a non-linear function of the number of synapses (see Eq. (1)) and therefore the proportion of synapses that contacts excitatory targets  $\Delta$  depends on the number of neurons in the presynaptic and the two postsynaptic populations ( $N^{pre}$ ,  $N^{post=e}$  and  $N^{post=i}$ ) as well as on the total number of synapses  $K$  and the desired target specificity  $T$ . In *Materials and Methods*, we provide the solution for  $\Delta$  assuming the linear approximation  $C = K / (N^{pre} N^{post})$ . The exact value is found by numerically solving

$$\begin{aligned} 2T &= \left(1 - \frac{1}{N^{post=i} N^{pre}}\right)^{(1-\Delta)K} (1 + T) \\ &\quad - \left(1 - \frac{1}{N^{post=e} N^{pre}}\right)^{\Delta K} (1 - T) \end{aligned} \quad (12)$$

for  $\Delta$ . In practice, we use this variant in order to prevent inaccuracies due to the approximation if  $K / (N^{pre} N^{post})$  is not sufficiently small.

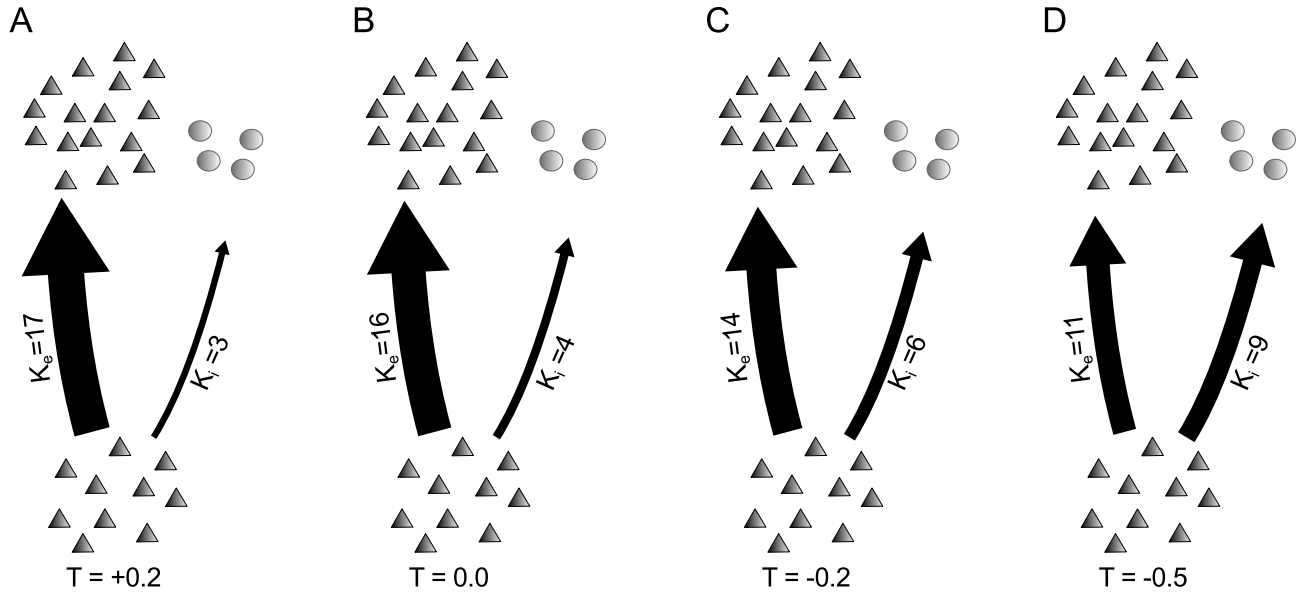


**Figure 13:** Redistribution of synapses with conserved total number of synapses according to eq. (12). The cartoons depict a situation with  $N^{\text{pre}} = 10$  presynaptic neurons (bottom triangles),  $N^{\text{post}=e} = 16$  excitatory (top triangles) and  $N^{\text{post}=i} = 4$  inhibitory (circles) postsynaptic neurons and  $K = 20$  synapses forming the projection of the presynaptic population to the postsynaptic layer. The arrow thickness corresponds to the indicated number of synapses that select excitatory ( $K_e$ ) and inhibitory ( $K_i$ ) targets. (A) Due to the larger dendritic length of the postsynaptic excitatory neurons, the application of Peters' rule results in a preferential targeting of excitatory neurons with a target specificity of at least  $T = +0.2$  (Fig. 4). (B) Random selection of postsynaptic neurons as it is typically applied in mono-layered network models (e.g. Brunel (2000b)). (C) and (D) show preferential selection of inhibitory targets with a target specificity of  $T = -0.2$  and  $T = -0.5$ , respectively.

## Selection of additional candidates for specific target type selection

Electrophysiological recordings (Thomson et al., 2002) demonstrated that the projection from L2/3e to L4 exclusively targets interneurons. We are not aware of further studies that investigate the inputs from L2/3 to L4 inhibitory cells. However, no further study in visual or somatosensory areas found connections from L2/3e to L4e, but connections in the inverse direction were reported from L4e to L2/3e (see Table 5). Only in auditory cortex, projections from L2/3e to L4e have been reported to pyramids and star pyramids (Barbour & Callaway, 2008).

The projection from L5e to L2/3 has a large scaling factor (Fig. 2) and evidence exists from several studies that this projection targets specifically inhibitory neurons in L2/3: Strongest evidence comes from a photostimulation study (Dantzker & Callaway, 2000) reporting that L2/3e cells receive few inputs from L5e while a subset of L2/3 inhibitory neurons receives the majority of its inputs from this layer. For the inputs from deep L5, only the input to this type of interneurons is significant at all. Yet, no paired recordings study reports measurements of the L5e to L2/3i connection, but several studies report an asymmetry of the feed-forward L2/3e to L5e and the inverse L5e to L2/3e connection (Thomson & Bannister, 1998; Thomson et al., 2002: ten-fold higher feed-forward connectivity, Lefort et al., 2009: 3.6-fold higher feed-forward connectivity). In contrast, the anatomical estimate provides similar probabilities for both connections and, in addition to Binzegger et al. (2004) which is based on a single reconstructed L5e axon projecting to L2/3, several studies found L5e cells predominantly projecting to L2/3 (e.g. Martin & Whitteridge, 1984; Stepanyants et al., 2008). These discrepancies between physiological and anatomical estimates can partly be related to undersampling of cells projecting to L2/3 in physiological recordings and also to stronger cutting of ascending axons in slice experiments: Stepanyants et al. (2009) estimated that only 60% of all potential connections can be expected to be intact for the excitatory L5 to L2/3 connection in paired recordings in slices. A refinement of our model that takes into account multiple excitatory L5 populations (e.g. L5A and L5B, see Schubert et al., 2006) can potentially resolve some of the connectivity observed on a finer scale. Taken together, this evidence qualifies the L5e to L2/3 projection as an i-specific candidate projection.

Zarrinpar & Callaway (2006) investigated the layer-specific input to L6 pyramids and interneurons in photostimulation experiments in rat primary visual cortex. Although the inputs from L2/3 to L6 are found to be sparse, they are significantly preferring interneuronal targets: in only very few cases (less than 10%) significant excitatory inputs from L2/3 to L6 pyramids are found, but in around 70% of all trials to interneurons (see their figure 5).

McGuire et al. (1984) find in an electron microscopy (EM) study that asymmetric (excitatory) synapses originating in L6 preferentially target the shafts of dendrites in L4. We include this projection as a candidate for specific target type selection inspite of the few samples underlying this study and the indirect assessment of connectivity without explicit identification of the postsynaptic cell. This interpretation of the EM data is partly supported by a similar case in the literature: White & Keller (1987) and Elhanany & White (1990) applied EM to study the connections of L6 cortico-cortical (CC) and cortico-thalamic (CT) cells and found that CT cells target predominantly dendritic shafts (as the L6e to L4 projection in McGuire et al. (1984)) while CC cells target spines as typical for excitatory cells (Braitenberg & Schüz, 1998). Later, paired recordings (Mercer et al., 2005; West et al., 2006) showed that this ultrastructural feature indeed reflects specific target

type selection of interneurons. Since primarily CT cells project to L4 (Briggs, 2010) it is possible that these cells show the same target type selection in this layer as in L6. Although the evidence is rather sparse (see also *Discussion*), we include also this projection in the list of i-specific candidates.

For the simulations, our reference parametrization assumes that the target specificity of the i-specific projections is  $-0.8$  for the projection from L2/3e to L4 and  $-0.4$  for the three other candidate projections.

### Algorithmic compilation of integrated connectivity map

(i) Input:

- (a)  $C_a = 1 - \left(1 - \frac{1}{N^{pre}N^{post}}\right)^K$
- (b)  $C_p = \sum_i R_i Q_i / (\sum_j Q_j)$
- (c) define  $r_m$  (here  $1 \text{ mm}^2$ )
- (d) define amendment candidates for target specificity  $T$  (Table 2)

(ii) Scale connection matrices

- (a)  $\sigma = r_p \left[ -2 \ln \left( 1 - \frac{\tilde{C}_p}{\tilde{C}_a} \right) \right]^{-1/2}$
- (b)  $C_0 = \frac{\tilde{C}_a}{2\pi\sigma^2}$
- (c)  $\bar{C}_m = \frac{2}{r_m^2} C_0 \sigma^2 [1 - \exp(-r_m^2 / (2\sigma^2))]$
- (d)  $C_{a/p} \leftarrow C_{a/p} \bar{C}_m / \bar{C}_{a/p}$

(iii) Redistribute synapses of anatomical map

- (a) solve [eq. \(12\)](#) for  $\Delta$
- (b)  $C_a^{\text{post}=e} \leftarrow 1 - \left(1 - \frac{1}{N^{pre}N^{post}}\right)^{\Delta K}$  (inhibitory connections analogously)

(iv) Correct target specificity of physiological map

- (a)  $C_p^{\text{post}=i(e)} \leftarrow \left(\frac{1-T}{1+T}\right)^{+(-1)} C_p^{\text{post}=e(i)}$
- (v)  $C_m = \frac{1}{2}(C_a + C_p)$

### Gray-matter long-range inputs

In order to estimate the layer-specific number of external gray-matter inputs  $K_{\text{ext}}^{\text{gm}}$ , we first define the relative number of external gray-matter connections as  $\gamma_{\text{ext}} = K_{\text{ext}}^{\text{gm}} / K_{\text{total}}^{\text{gm}}$ , where the total number of gray-matter connections can be divided into local and external connections  $K_{\text{total}}^{\text{gm}} = K_{\text{local}} + K_{\text{ext}}^{\text{gm}}$ . Here, we assume that the relative number of external gray-matter connections  $\gamma_{\text{ext}}$  corresponds to the weighted and normalized number of bouton clusters located outside of the local cortical network as measured by [Binzegger et al. \(2007\)](#). The weighted and normalized number of non-local bouton clusters is defined as follows: we count the number of bouton clusters  $\xi_\rho$  with a horizontal displacement greater than  $0.56 \text{ mm}$  (i.e. outside of the local cortical volume below  $1 \text{ mm}^2$  of cortical surface) in [Binzegger et al. \(2007\)](#), their figure 11, according to the rank  $\rho \in \{1, 2, 3\}$  (where

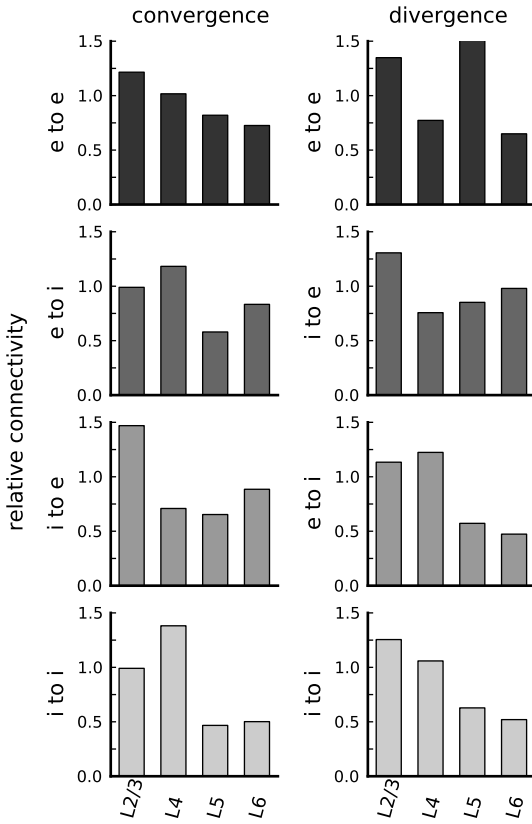


**Figure 14:** Relative connectivity of the four connection types. The relative convergent (left column) connectivity is the ratio of the relative averaged convergence (weighted according to neuronal densities of postsynaptic cell types) and the relative neuronal densities of the presynaptic cell types. The relative divergent (right column) connectivity is defined analogously for divergence. The relative connectivity can be used to determine, which layer plays the dominant role in the local network: If the overall effect of a neuron would be independent of its layer, any neuron in the network, on average, sampled randomly from all other neurons and the layer specificity of the average convergence and divergence corresponded to the distribution of the number of neurons (relative connectivity of 1). We find that neurons do not sample randomly from all other neurons in the network, for different connection types, different layers play the dominant role: the highest number of excitatory inputs relative to neuron numbers (to excitatory and inhibitory targets) originates from L2/3, inhibitory inputs (again to both target types) from L4. Fewest inputs relative to neuron numbers are provided by L6 (e to e) and L5 (all other connection types). For outputs, the situation is different: the highest number of outputs relative to neuron numbers are projected to L5 (e to e), to L4 (e to i) and to L2/3 (i to e/i). Fewest outputs relative to neuron numbers are projected to L4 (i to e) and to L6 (all other types).

	L2/3e	L4e	L5e	L6e
number of external clusters $\xi_1$	1	2	1	0
number of external clusters $\xi_2$	2	1	0	1
number of external clusters $\xi_3$	9	1	1	2
number of clusters $\Xi_{\text{total}}$	24	18	6	14
cluster weight $\omega_1$	0.65	0.75	0.55	0.75
cluster weight $\omega_2$	0.18	0.2	0.25	0.2
cluster weight $\omega_3$	0.17	0.05	0.2	0.05
number of local connections $k_{\text{local}}$	4512	3277	2721	2702
number of gray-matter inputs $k_{\text{ext}}^{\text{gm}}$	534	353	389	79
number of thalamic inputs	0	93	0	47
number of white-matter inputs	1072	1665	1609	2790
total number of external inputs $k_{\text{ext}}^{\text{total}}$	1606	2111	1997	2915

**Table 6:** Layer-specific external input properties. From top to bottom: the extracted parameters required to calculate the number of gray-matter external connections, the estimates of the three types of external inputs (gray-matter, thalamic and white-matter) to excitatory neurons, and the total number of external inputs. The total number of external inputs is rounded for simulations (compare Table 4).

rank 3 collapses rank  $> 2$ ). The relative number of external bouton clusters is calculated by dividing  $\xi_\rho$  by the total number of clusters  $\Xi_{\text{total}}$  that can be extracted from [Binzegger et al. \(2007\)](#), their figure 3B. In order to assess the relative proportion of synapses formed by neurons outside of the local cortical network, we multiply the relative number of external bouton clusters with the cluster weights  $\omega_\rho$  that can be extracted from [Binzegger et al. \(2007\)](#), their figures 4C and 4D for rank  $\rho = 1$  and 2. As an estimate for rank 3 we use the remaining weight  $\omega_3 = 1 - (\omega_1 + \omega_2)$ . Finally, we sum over all ranks and obtain with

$$\gamma_{\text{ext}} = \sum_{\rho=1}^3 \xi_\rho \omega_\rho / \Xi_{\text{total}}$$

for the number of external gray-matter inputs:

$$\begin{aligned} K_{\text{ext}}^{\text{gm}} &= K_{\text{local}} \frac{\gamma_{\text{ext}}}{1 - \gamma_{\text{ext}}} \\ &= K_{\text{local}} \frac{\sum_{\rho=1}^3 \xi_\rho \omega_\rho}{\Xi_{\text{total}} - \sum_{\rho=1}^3 \xi_\rho \omega_\rho}. \end{aligned}$$

The total number of layer-specific external inputs  $K_{\text{ext}}$  then is the sum of the external gray-matter inputs  $K_{\text{ext}}^{\text{gm}}$ , the extrinsic (white-matter,  $\text{wm}$ ) inputs  $K_{\text{ext}}^{\text{wm}}$  and specific thalamic inputs  $K_{\text{ext}}^{\text{th}}$ . [Table 6](#) contains detailed information on the extracted values for all parameters of external inputs.

### Cell-type specific input structure

To visualize the strongest pathways in the cell-type specific input structure we calculate a input hierarchy. Therefore, we consider the graph  $G = (V, E)$  with the neuronal populations as vertices  $V = \{\text{L2/3e}, \text{L2/3i}, \text{L4e}, \text{L4i}, \text{L5e}, \text{L5i}, \text{L6e}, \text{L6i}\}$  and the edges  $E = \{(v, w) | C((v, w)) > 0.04\}$  being those connections with connection probabilities  $C$  greater than 0.04. In the input hierarchy, the first

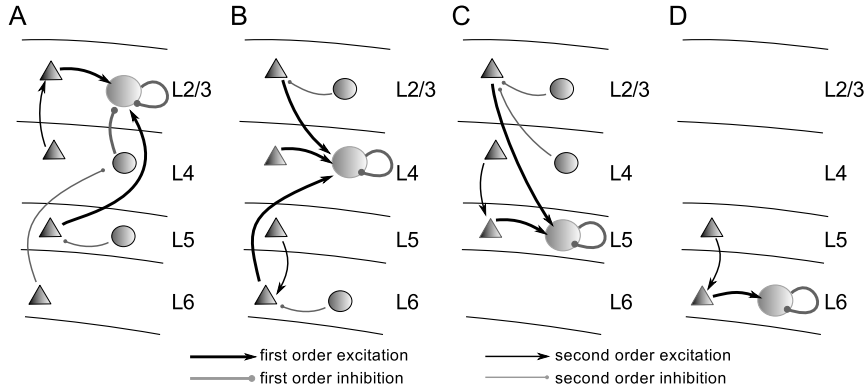


**Figure 15:** Differences in input structure for inhibitory cell types L2/3i (A), L4i (B), L5i (C) and L6i (D) (large circles). The illustrations show the strongest pathways of direct (first-order, thick arrows) and indirect (second-order, thin arrows) excitation (black) and inhibition (gray) of a given population. Triangles represent excitatory and circles represent inhibitory populations.

order inputs to a vertex  $w$  are defined as the direct inputs

$$L_1(w) = \{v | (v, w) \in E\}.$$

The second order inputs to  $w$  are the strongest of the direct inputs to the elements in  $L_1(w)$ :

$$\begin{aligned} L_2(w) = & \{v | \exists v \in V \setminus L_1(w) \\ & \cap \exists w' \in L_1(w) : (v, w') \in E \\ & \cap \forall w'' \in L_1(w) \setminus \{w'\} : C((v, w'))C((w', w)) > C((v, w''))C((w'', w))\}. \end{aligned}$$

The definition can easily be extended to higher order inputs. Second and higher order inputs are excitatory (inhibitory) if the product of mean synaptic strengths in the pathway is positive (negative).

### Wiring algorithm

The time consumption of the serial wiring algorithm described in Fig. 16A is  $\mathcal{O}(K)$ . In a distributed simulation setup (Fig. 16B), the neurons are distributed over  $M$  processes and the synapses are only created on the process where the postsynaptic neuron is located. In this case, the high-level connection routine for randomly connecting neuronal populations is as follows: Let  $M$  be the number of processes,  $K$  the number of synapses to create,  $\mathbf{N}^{\text{pre}(\text{post})}$  the arrays containing all global identifiers (GIDs) of the presynaptic (postsynaptic) neurons and  $\mathbf{N}_M^{\text{post}}$  the distribution of postsynaptic neurons on processes, i.e.  $\mathbf{N}_M^{\text{post}}[m]$  contains all GIDs of postsynaptic neurons located on the  $m$ th process. The numbers of synapses created on a given process  $\mathbf{K}_M$  is binomially distributed (because of the uniform probability that a synapse is established on a given machine) with the boundary condition that the total number of connections is  $K = \sum_m \mathbf{K}_M[m]$ , i.e.  $\mathbf{K}_M$  is multinomially distributed. In order to optimize the parallelization of the high-level connection routine, we draw a priori a random sample  $\mathbf{K}_M$  from the multinomial distribution depending on  $K$ ,  $M$  and  $\mathbf{N}_M^{\text{post}}$  (Davis, 1993). This sample has to be identical on every process, which can be achieved by the usage of an identically

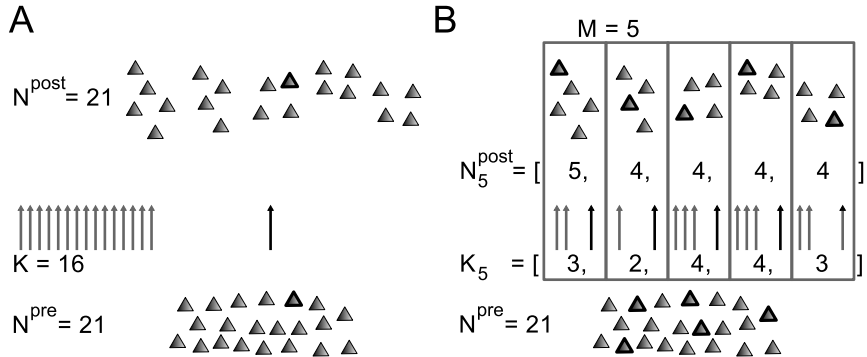


**Figure 16:** Wiring algorithm. The cartoons depict the presynaptic (bottom triangles) and the postsynaptic (top triangles) populations, here both containing  $N^{\text{pre}}(N^{\text{post}}) = 21$  neurons. The connection probability between the two populations is  $C = 0.357$ , corresponding to  $K = 16$  synapses (arrows, black indicating the currently established synapses). (A) Serial version. For every synapse, the pre- and postsynaptic neuron (highlighted triangles) are drawn from the corresponding populations. (B) Distributed version. The network is distributed over  $M = 5$  processes (gray boxes) such that the first process hosts  $N_5^{\text{post}}[0] = 5$  postsynaptic neurons and all other processes 4 postsynaptic neurons. The number of synapses on each process (here  $\mathbf{K}_M = [3, 2, 4, 4, 3]$ ) is multinomially distributed. The algorithm can establish 5 connections in parallel (black arrows and highlighted triangles).

seeded random number generator. To create the synapses, we draw (on process  $m$  and using independent random number generators on every process)  $\mathbf{K}_M[m]$  times a presynaptic neuron  $j$  from  $\mathbf{N}^{\text{pre}}$  and a postsynaptic neuron  $i$  from  $\mathbf{N}_M^{\text{post}}[m]$  as well as the synaptic weight  $w_{ij}$  and delay  $d_{ij}$  from the gaussian distributions and call the low-level function  $\text{Connect}(i, j, w_{ij}, d_{ij})$ . Fig. 16B shows that the presynaptic neuron is drawn from all neurons in the presynaptic population, but that the postsynaptic neuron on a given process is drawn only from postsynaptic neurons located on this process.

The algorithm requires a small serial overhead in order to create the distribution of the postsynaptic neurons over processes and the random sample from the multinomial distribution. Else, it guarantees that on every process, only calculations are carried out that are required to create synapses local to the process, i. e. the time consumption is  $\mathcal{O}(K/M)$ .

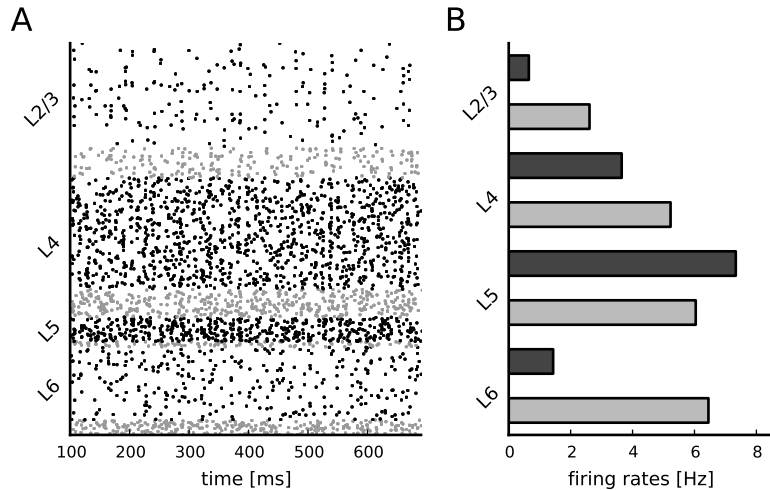


**Figure 17:** Replacing the Poissonian background noise with constant input currents to all neurons yields basically the same activity, demonstrating that the external noise is not requirement for the asynchronous irregular firing. The raster plot (A) exhibits only slightly more synchrony than the simulation with Poissonian background (Fig. 7A). The input current to the different populations is chosen identical to the mean input current evoked by the Poissonian background input in the reference parametrization (Table 4). The resulting firing rates (B) are the same as in Fig. 7B.

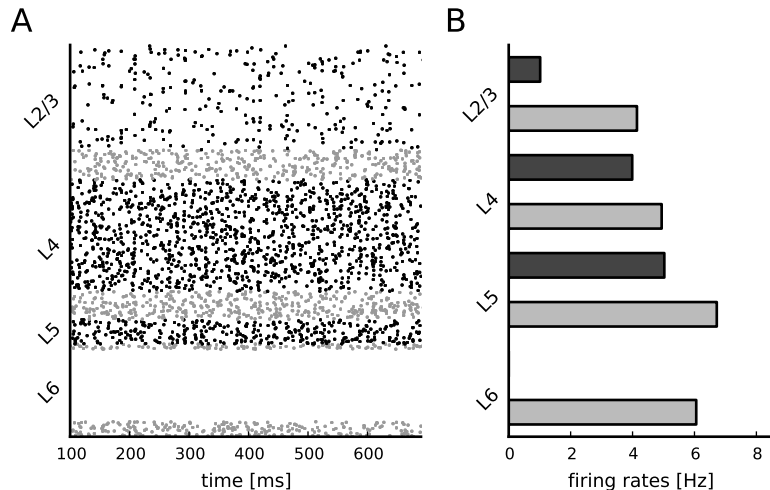


**Figure 18:** The network simulations exhibit comparable spontaneous activity features when the external inputs are independent of the layer. (A) shows the raster plot and (B) the cell-type specific firing rates after replacing the estimated numbers of external inputs  $k_{\text{ext}}$  with  $k_{\text{ext}}^{\text{hom}} = 2000$  for excitatory populations and  $k_{\text{ext}}^{\text{hom}} = 1850$  for inhibitory populations. The order of firing rates is basically the same as with data based external inputs: L2/3e and L6e exhibit lowest, L4e intermediate and L5e highest rates; inhibitory rates are higher than excitatory ones. L6e is basically silent. This is due to the small excitatory input to the excitatory population: the data based estimate assigns 50% more inputs to this population.

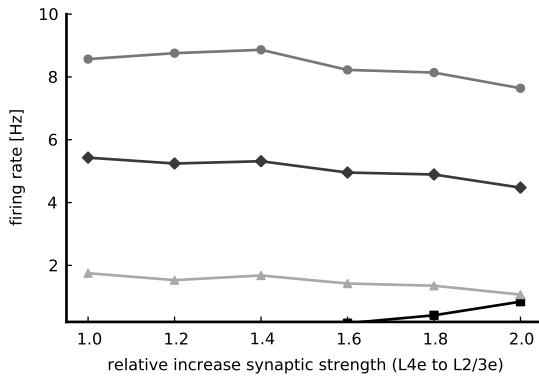


**Figure 19:** Dependence of stationary activity on the synaptic strength of the L4e to L2/3e connection. The available experimental data do not constrain the connection probabilities between L4 and L2/3 unambiguously (see also *Discussion*). [Feldmeyer et al. \(2006\)](#) find that the convergence onto L2/3 pyramids from other L2/3 pyramids and from L4 cells is the same. In our model, however, the convergence from L2/3 cells is twice as large as from L4. To test for the influence of this connection, we increase the synaptic strength of the L4e to L2/3e connection. The graph shows the firing rates of the excitatory populations in L2/3 (squares), L4 (diamonds), L5 (circles) and L6 (triangles), lightness increases with depth as a function of the relative increase of this synaptic strength. L2/3e fires a significant number of spikes for an increase of  $> 1.6$ . The other layers are only slightly affected by this modification. An increase of 2 is consistent with the relative convergence described by [Feldmeyer et al. \(2006\)](#) and corresponds to our reference parametrization.

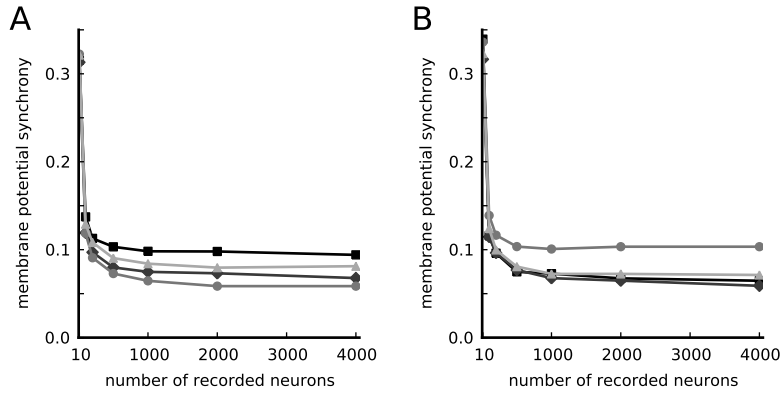


**Figure 20:** Membrane potential synchrony according to (Golomb, 2007). The graphs shows the membrane potential synchrony of (A) excitatory populations and (B) inhibitory populations in L2/3 (squares), L4 (diamonds), L5 (circles) and L6 (triangles), lightness increases with depth, as a function of the number of recorded membrane potential traces. The membrane potential synchrony  $\chi$  depends on the number of neurons  $N$  as  $\chi(N) = \chi(\infty) + \frac{a}{\sqrt{N}} + \mathcal{O}(N)$  where  $a > 0$  is a constant (Golomb, 2007). As known from previous studies on mono-layer models (Brunel, 2000b), the asynchronous activity is not perfectly asynchronous (which would correspond to  $\chi(\infty) = 0$ ), but weakly synchronized. In the layered network model, the subthreshold activity is similar, with  $\chi(\infty) \approx 0.1$ . The membrane potential synchrony of excitatory neurons is ordered as follows (from largest to smallest values): L2/3e, L6e, L4e, L5e. For inhibitory neurons it is highest in L5i and almost identical in the other layers.

Table 7: Numerical connectivity values. From left to right: connection specifier, physiological connection probability estimates for raw and modified data, anatomical estimates for the number of synapses (in billion) and the corresponding connection probabilities for raw and modified data sets, respectively. A dash (–) indicates connections that have not been measured. Non-zero but undetermined values of the raw physiological data set are given with the estimates used by Haeusler & Maass (2007) in brackets.

connection	$C_p^{\text{raw}}$	$C_p^{\text{mod}}$	$K_a^{\text{raw}}$	$K_a^{\text{mod}}$	$\tilde{C}_a^{\text{raw}}$	$\tilde{C}_a^{\text{mod}}$
L2/3e → L2/3e	0.223	0.122	73.6	73.6	0.172	0.172
L2/3e → L2/3i	0.212	0.416	10.3	10.3	0.086	0.086
L2/3i → L2/3e	0.182	0.413	16.7	20.3	0.139	0.169
L2/3i → L2/3i	0.4	0.4	2.9	3.4	0.086	0.101
L4e → L4e	0.174	0.122	23.5	23.5	0.05	0.05
L4e → L4i	0.19	0.282	3.5	3.5	0.029	0.029
L4i → L4e	0.095	0.304	10.8	18.0	0.09	0.15
L4i → L4i	0.5	0.5	1.9	2.9	0.065	0.098
L5e → L5e	0.092	0.122	3.1	3.1	0.13	0.13
L5e → L5i	0.096	0.109	0.42	0.42	0.081	0.081
L5i → L5e	0.123	0.194	0.42	4.0	0.082	0.781
L5i → L5i	0.6	0.6	0.07	0.47	0.062	0.414
L6e → L6e	–	–	15.7	15.7	0.075	0.075

connection	$C_p^{\text{raw}}$	$C_p^{\text{mod}}$	$K_a^{\text{raw}}$	$K_a^{\text{mod}}$	$\tilde{C}_a^{\text{raw}}$	$\tilde{C}_a^{\text{mod}}$
L6e→L6i	–	–	1.4	1.4	0.032	0.032
L6i→L6e	–	–	–	11.4	–	0.269
L6i→L6i	–	–	–	1.5	–	0.173
L2/3e→L4e	0.0	0.0	9.2	9.2	0.02	0.02
L2/3e→L4i	0.163	0.163	0.95	0.95	0.008	0.008
L2/3i→L4e	0.0	0.0	1.8	1.8	0.014	0.014
L2/3i→L4i	0.0	0.0	0.22	0.22	0.007	0.007
L2/3e→L5e	0.58	0.180	12.3	12.3	0.123	0.123
L2/3e→L5i	0.0	0.0	1.5	1.5	0.067	0.067
L2/3i→L5e	>0.0(0.2)	>0.0(0.2)	0.84	0.84	0.03	0.03
L2/3i→L5i	>0.0(0.0)	>0.0(0.0)	0.08	0.08	0.013	0.013
L2/3e→L6e	–	–	9.2	9.2	0.031	0.031
L2/3e→L6i	–	–	0.26	0.26	0.004	0.004
L2/3i→L6e	–	–	0.66	0.66	0.008	0.008
L2/3i→L6i	–	–	0.02	0.02	0.001	0.001
L4e→L2/3e	0.147	0.112	18.4	18.4	0.041	0.041
L4e→L2/3i	0.098	0.098	2.6	2.6	0.02	0.02
L4i→L2/3e	0.327	0.327	0.96	0.96	0.008	0.008
L4i→L2/3i	>0.0(0.2)	>0.0(0.2)	0.17	0.17	0.005	0.005
L4e→L5e	0.0	0.14	3.7	3.7	0.035	0.035
L4e→L5i	0.0	0.0	0.42	0.42	0.018	0.018
L4i→L5e	0.0	0.0	0.36	0.36	0.014	0.014
L4i→L5i	0.0	0.0	0.03	0.03	0.005	0.005
L4e→L6e	–	–	7.8	7.8	0.025	0.025
L4e→L6i	–	–	0.26	0.26	0.004	0.004
L4i→L6e	–	–	1.6	1.6	0.02	0.02
L4i→L6i	–	–	0.01	0.01	0.001	0.001
L5e→L2/3e	0.034	0.014	8.9	8.9	0.089	0.089
L5e→L2/3i	0.0	0.0	1.3	1.3	0.045	0.045
L5i→L2/3e	0.0	0.0	0.0	0.0	0.0	0.0
L5i→L2/3i	0.0	0.0	0.0	0.0	0.0	0.0
L5e→L4e	0.0	0.0	1.7	1.7	0.016	0.016
L5e→L4i	0.0	0.0	0.21	0.21	0.008	0.008
L5i→L4e	0.0	0.0	0.18	0.18	0.001	0.001
L5i→L4i	0.0	0.0	0.0	0.0	0.0	0.0
L5e→L6e	–	–	4.8	4.8	0.068	0.068
L5e→L6i	–	–	0.47	0.47	0.033	0.033
L5i→L6e	–	–	0.36	0.36	0.024	0.024
L5i→L6i	–	–	0.03	0.03	0.01	0.01
L6e→L2/3e	–	–	2.7	2.7	0.009	0.009
L6e→L2/3i	–	–	0.42	0.42	0.005	0.005
L6i→L2/3e	–	–	–	0.0	–	0.0
L6i→L2/3i	–	–	–	0.0	–	0.0
L6e→L4e	–	–	37.2	37.2	0.12	0.12
L6e→L4i	–	–	5.7	5.7	0.072	0.072
L6i→L4e	–	–	–	0.0	–	0.0
L6i→L4i	–	–	–	0.0	–	0.0
L6e→L5e	–	–	1.7	1.7	0.024	0.024
L6e→L5i	–	–	0.16	0.16	0.01	0.01

connection	$C_p^{\text{raw}}$	$C_p^{\text{mod}}$	$K_a^{\text{raw}}$	$K_a^{\text{mod}}$	$\tilde{C}_a^{\text{raw}}$	$\tilde{C}_a^{\text{mod}}$
L6i→L5e	–	–	–	0.0	–	0.0
L6i→L5i	–	–	–	0.0	–	0.0
mean values	0.145	0.139	–	–	0.046	0.079